nature biomedical engineering

Article

https://doi.org/10.1038/s41551-023-01149-4

Ultrafast longitudinal imaging of haemodynamics via single-shot volumetric photoacoustic tomography with a single-element detector

In the format provided by the authors and unedited

Contents

Supplementary Note 1 | Fly's eye homogenizer in PACTER.
We use a fly's eye homogenizer to provide uniform illumination for PACTER[74]. As shown in **Supplementary Fig. 2**, the two microlens arrays form multiple parallel Köhler illumination systems side-by-side. The original beam entering the first microlens array is divided into multiple beamlets. Through the lenslets pairs in the microlens arrays and the spherical lens, each beamlet of the original beam is imaged to the homogenization plane, i.e., the top of the ER. Because the images of the beamlets are all superimposed on the homogenization plane, the intensity differences among the beamlets disappear in their superimposed images. Therefore, the intensity distribution of the homogenized beam is independent of the homogeneity of the original beam. Further, the square-type microlens arrays in the setup will generate a square flat-top intensity distribution in the homogenization plane, which provides a good match for the square-type calibration pattern in PACTER, allowing accurate mapping between the calibration and imaging areas.

The width of the homogenized beam, d_H, is given by

$$d_H = \frac{p_M f_L (2f_M - a)}{f_M^2}, \tag{S1}$$

where p_M and f_M are the pitch and focal length of the lenslets in the two identical microlens arrays, f_L is the focal length of the spherical lens, and a is the separation between the microlens arrays. In PACTER, a is set to be identical to f_M, leading to

$$d_H = \frac{p_M f_L}{f_M}. \tag{S1}$$

The divergence half-angle after the homogenization plane, θ, is given by

$$\theta = \operatorname{atan}\left(\frac{d_O + d_H - p_M}{2f_L}\right), \tag{S2}$$

where d_O is the diameter of the original beam. In PACTER, we use the microlens arrays with $p_M = 0.5\ \mathrm{mm}$ and $f_M = 15\ \mathrm{mm}$, the spherical lens with $f_L = 250\ \mathrm{mm}$, and the original beam with a diameter of $d_O = 6\ \mathrm{mm}$. Therefore, the homogenized beam has a width of $d_H \approx 8\ \mathrm{mm}$, matching the size of the calibration pattern (80 by 80 steps with a step size of 0.1 mm), and the divergence half-angle $\theta \approx 2°$. The small divergence ensures homogenous illumination across the whole 3D volume ($8\ \mathrm{mm} \times 8\ \mathrm{mm} \times 3.6\ \mathrm{mm}$) for *in vivo* imaging. Within the 3.6 mm depth, the illumination beam merely diverges laterally by 0.13 mm, which is much smaller than the lateral resolution (0.56 mm) of PACTER. Hence, the beam divergence within the imaging volume can be ignored.

Supplementary Note 2 | Universal calibration of PACTER.
Recently, we developed photoacoustic topography through an ergodic relay (PATER), which captured a wide-field PA image with a single laser shot using a single-element ultrasonic transducer[38–40]. However, PATER suffered from the following limitations. (1) PATER could only image a 2D projection of the object, unable to capture a tomographic image in 3D. (2) The ER in PATER had to be re-calibrated for each different object; because the calibration relied on a point-by-point scanning of a laser beam, the imaging procedure was time-consuming. (3) PATER required that the boundary conditions of the object and the ER stay unchanged throughout the experiment and thus could not be used for long-term imaging in unstable environments.

One major distinction between PATER and PACTER lies in the structures of their ERs. In PATER, the ER is simply a prism (**Supplementary Fig. 8a**). After a PA signal is generated from the object (t_0) and detected by the transducer (t_1), it quickly propagates to and reflects from the boundary between the object and the ER (t_2), as shown in the simulation based on the *k*-wave toolbox[75] (**Supplementary Fig. 8b**). Once the boundary condition between the object and the ER changes because of movements of the object, instability of the system, or switching to a different object, the signal will also change. Therefore, if the ER is calibrated with one object, e.g., bovine blood, and then used to image a different object, e.g., a black wire, the reconstruction will fail (**Supplementary Fig. 8c**). In other words, the PATER signal is strongly object-dependent (**Supplementary Fig. 8d**), and it requires that the boundary conditions of the object and the ER remain unchanged throughout the experiment.

In comparison, the ER of PACTER consists of a prism and a fused silica rod, where the rod functions as an acoustic delay line that temporally separates the initial and reflected PA signals[41] (**Supplementary Fig. 8e**). When a PA signal is generated from the object (t_0) and detected by the ultrasonic transducer (t_1), a part of the acoustic signal is trapped and scrambled in the prism, whereas the other part is reflected toward the object and then reverberated to the transducer (t_2), as denoted by the black dotted arrows in the simulation (**Supplementary Fig. 8f**). Because only the reflected part of the acoustic signal will be affected by the boundary condition between the object and the ER, once this part is excluded from the measurement, the acquired signal will be object-independent. Consequently, the ER can be used to image any object, e.g., a black wire, despite it has been calibrated only once using a different object, e.g., bovine blood (**Supplementary Fig. 8g**). Whereas almost the whole PATER signal is object-dependent (**Supplementary Fig. 8d**), a large segment (>100 μs) of the PACTER signal is object-independent (**Supplementary Fig. 8f**), enabling universal calibration in PACTER despite its 3D imaging capability (**Supplementary Video 2**). It should be noted that the long duration of the signals poses a limit on the maximum laser repetition rate, i.e., the volumetric imaging rate, the system can support. For instance, if the duration of the signal is longer than 250 μs, the laser repetition rate should be lower than 4 kHz.

Supplementary Note 3 | Forward model and image reconstruction.
We performed calibrations at pixels on a 2D plane and used these pixels as virtual ultrasonic transducers for 3D imaging. If non-zero initial pressure exists only on the calibration plane, the detected signal $s(t)$ at time t can be expressed as

$$s(t) = \sum_{n=1}^{N} p_n k_n(t)\,, t \geq 0, \tag{S3}$$

where N is the number of calibrated virtual transducers, $k_n(t)$ is the normalized impulse response from the calibration at the n-th virtual transducer, and p_n is the root-mean-squared PA amplitude proportional to the initial pressure at the n-th virtual transducer.

For initial pressure in a 3D volume, we assume M source points located at $\mathbf{r}'_m, m = 1,2, \dots, M$, in an acoustically homogeneous 3D region attached to the calibration plane. The PA wave generated from the source point at $\mathbf{r}'_m$ propagates to the calibrated virtual transducer $\mathbf{r}_n$ with the speed of sound c after time $t_{m,n} = \frac{\|\mathbf{r}'_m - \mathbf{r}_n\|}{c}$, which, through the ER, adds $p_{m,n} k_n\left(t - \frac{\|\mathbf{r}'_m - \mathbf{r}_n\|}{c}\right)$ to the detected signal, with the PA amplitude $p_{m,n}$ quantified as $p_{m,n} = \frac{w(\theta_{m,n}) p_{0,m}}{\|\mathbf{r}'_m - \mathbf{r}_n\|}$. Here, $\theta_{m,n}$ denotes the incidence angle satisfying $\cos\theta_{m,n} = \frac{(\mathbf{r}'_m - \mathbf{r}_n)\cdot \mathbf{n}}{\|\mathbf{r}'_m - \mathbf{r}_n\|}$ with $\mathbf{n}$ being the normal vector of the calibration plane; function $w(\theta_{m,n})$ describes a virtual transducer's angle-dependent sensitivity; and $p_{0,m}$ is proportional to the initial pressure at $\mathbf{r}'_m$. We replace $p_n k_n(t)$ in Eq. (S3) with $p_{m,n} k_n\left(t - \frac{\|\mathbf{r}'_m - \mathbf{r}_n\|}{c}\right)$ from all the M source points and obtain the detected wide-field PA signal

$$s(t) = \sum_{n=1}^{N} \sum_{m=1}^{M} \frac{w(\theta_{m,n}) p_{0,m}}{\|\mathbf{r}'_m - \mathbf{r}_n\|} k_n\left(t - \frac{\|\mathbf{r}'_m - \mathbf{r}_n\|}{c}\right), t \geq 0. \tag{S4}$$

Here, we define $k_n(t) = 0,\ n = 1,2 \dots, N,\ t < 0$. For sufficiently small virtual ultrasonic transducers, we assume that

$$w(\theta_{m,n}) = \mathbf{1}_{[0,\theta_1]}(\theta_{m,n}) \cos\theta_{m,n}\,. \tag{S5}$$

Here, we use the indicator function

$$\mathbf{1}_A(x) = \begin{cases} 1, x \in A \\ 0, x \notin A \end{cases} \tag{S6}$$

to rejection detections with incidence angles greater than the critical angle θ_1 (quantified in **Supplementary Note 4**). Substituting Eq. (S5) into Eq. (S4) yields

$$s(t) = \sum_{n=1}^{N} \sum_{m=1}^{M} p_{0,m} \frac{\mathbf{1}_{[0,\theta_1]}(\theta_{m,n}) \cos\theta_{m,n}}{\|\mathbf{r}'_m - \mathbf{r}_n\|} k_n\left(t - \frac{\|\mathbf{r}'_m - \mathbf{r}_n\|}{c}\right), t \geq 0. \tag{S7}$$

We let L be the number of time points after temporal discretization. Then the computational complexity of a forward model based on Eq. (S7) is $O(MNL)$.

To accelerate the forward model in Eq. (S7), we split the delay term $\frac{\|\mathbf{r}'_m - \mathbf{r}_n\|}{c}$ from function $k_n(t)$ through temporal convolution:

$$k_n\left(t - \frac{\|\mathbf{r}'_m - \mathbf{r}_n\|}{c}\right) = \delta\left(t - \frac{\|\mathbf{r}'_m - \mathbf{r}_n\|}{c}\right) * k_n(t), m = 1,2, \dots, M, n = 1,2, \dots, N, t \geq 0. \tag{S8}$$

Substituting Eq. (S8) into Eq. (S7), we obtain

$$s(t) = \sum_{n=1}^{N} k_n(t) * \sum_{m=1}^{M} p_{0,m} \frac{\mathbf{1}_{[0,\theta_1]}(\theta_{m,n}) \cos\theta_{m,n}}{\|\mathbf{r}'_m - \mathbf{r}_n\|} \delta\left(t - \frac{\|\mathbf{r}'_m - \mathbf{r}_n\|}{c}\right), t \geq 0. \tag{S9}$$

The inner summation in Eq. (S9) has a complexity of $O(MN)$ and each temporal convolution is implemented through three fast Fourier transforms (FFTs) with a complexity of $O(L\log_2 L)$. Thus, the forward model based on Eq. (S9) has a computational complexity of $\max\{O(MN), O(NL\log_2 L)\}$.

We perform numerical simulations to quantify the improvement of computational efficiency brought by the fast algorithm. Considering that the complexities of both the slow (Eq. (S7)) and fast (Eq. (S9)) algorithms are linearly dependent on the number of virtual detectors N, we simplify the problem to a single virtual detector (N =1) with L = 65,536 and $M = 80 \times 80 \times 120$, and only consider the computation time of a forward simulation. In a Windows 11 Home system with Intel® Core™ i9-10900T CPU @ 1.90GHz, we perform single-CPU-core forward simulations based on the slow and fast algorithms, respectively, 36 times in Matlab. The average computation times of the simplified forward simulation are 20 s and 2.2×10^{-3} s (×9,100 acceleration), respectively, which correspond to 35.6 h and 14.1 s for a true forward simulation in this study ($N = 80 \times 80$).

Supplementary Note 4 | Spatial resolution analysis based on the virtual transducer array.
We analyze the anisotropy of the spatial resolution from two perspectives: one with an emphasis on the physical intuition (this Note), the other with an emphasis on the mathematical derivation (**Supplementary Note 5**). The two perspectives clarify the differences in value between the lateral and axial resolutions.

We first analyze the anisotropy of the spatial resolution by assuming that the PACTER signals detected by the single-element transducer are accurately decoded to the signals detected by the 80×80 virtual transducers. We use the spectrum of the PACTER signal detected by the integrated PMN-PT transducer (30-MHz central frequency) in **Supplementary Fig. 12a**, denoted as $\hat{s}(f)$, to approximate the detection spectrum of each virtual transducer element. From $\hat{s}(f)$, we obtain the central frequency $f_0 = \frac{\int_0^{f_\mathrm{m}} f|\hat{s}(f)|^2 \mathrm{d}f}{\int_0^{f_\mathrm{m}} |\hat{s}(f)|^2 \mathrm{d}f} \approx 8.3\ \mathrm{MHz}$ and the bandwidth $f_\mathrm{w} = \sqrt{\frac{\int_0^{f_\mathrm{m}} (f-f_0)^2 |\hat{s}(f)|^2 \mathrm{d}f}{\int_0^{f_\mathrm{m}} |\hat{s}(f)|^2 \mathrm{d}f}} \approx 12.2\ \mathrm{MHz}$, respectively[76]. Here, we set the upper frequency as $f_\mathrm{m} = 125\ \mathrm{MHz}$, which is the Nyquist frequency corresponding to the 250 MHz sampling rate. Additionally, the speed of sound in fused silica (longitudinal wave speed $c_\mathrm{l} = 5.9\ \mathrm{mm \cdot \mu s^{-1}}$)[77] is greater than that in water ($c = 1.5\ \mathrm{mm \cdot \mu s^{-1}}$)[78], leading to a critical angle (denoted at θ_l) of the ultrasonic wave's refraction from water into fused silica (**Supplementary Fig. 12b**). This leads to a limited-view effect in the proposed system: waves of incidence angels greater than the critical angle θ_l are totally reflected and not detected by the transducer. The critical angle satisfies $\sin\theta_\mathrm{l} = \frac{c}{c_\mathrm{l}} \approx 0.25$, which equals the numerical aperture (NA) of the virtual 2D array. Here, the longitudinal wave speed is used to quantify the critical angle due to the single-element transducer's dominant sensitivity to the longitudinal waves[79]. For the virtual 2D array, the axial resolution (along the *z*-axis) is quantified as $R_A = 0.88\frac{c}{f_w} \approx 0.11\ \mathrm{mm}$, while the lateral resolution (in the *x*-*y* plane) is quantified as $R_L = 0.71\frac{c}{NA \cdot f_0} \approx 0.51\ \mathrm{mm}$[13]. Both values are close to the measured axial (0.13 mm) and lateral (0.56 mm) resolutions shown in **Fig. 3g**. It is important to note that, if a post-fabrication transducer (10-MHz central frequency) is used, the central frequency f_0 and bandwidth f_w of the PACTER signal will be 5.0 MHz and 4.0 MHz, respectively (**Supplementary Fig. 7**). Consequently, the lateral and axial resolutions of PACTER will be 0.86 mm and 0.33 mm, respectively. Therefore, the integrated PMN-PT transducer with a 30-MHz central frequency is more suitable for PACTER.

The design of the integrated PMN-PT transducer incorporated an active aperture size of 0.4 × 0.4 mm^2. This decision was based on several factors. On one hand, it was essential for the transducer size to be relatively small to ensure that the acoustic waves could be effectively scrambled in the ER before being detected by the transducer. Conversely, if the transducer size is excessively small, only a minimal portion of the acoustic waves would be captured, potentially leading to a deterioration in SNR and a corresponding decrease in resolution[41]. Increasing the element size may compromise the scrambling but enhance the SNR, while decreasing the size has the opposite effects, both of which influence image resolution. In this study, a comprehensive analysis of the dependency of image resolution on element size was not conducted. Instead, through experimentation, we determined the element size of $0.4 \times 0.4\ \mathrm{mm}^2$ to be a suitable balance between sufficient scrambling and SNR, thereby ensuring high image quality.

Supplementary Note 5 | Spatial resolution analysis based on the system matrix.
Obtaining signals detected by all the virtual transducers is an ill-posed problem and we reconstruct an image directly from the single-element-detected signals. We iteratively invert the system matrix $\mathbf{H}$ (of size $L \times M$) to obtain the images, which manifest anisotropic resolutions (see Methods). To explain the anisotropy in theory, we analyze the gradient matrix $\mathbf{H}^{\mathrm{T}}\mathbf{H}$, whose property eventually determines the image resolution in the iterative method. The m-th column of $\mathbf{H}$ is a temporally discretized form of the following transducer's response to the point source at $\mathbf{r}'_m$:

$$s_m(t) = \sum_{n=1}^{N} \frac{\mathbf{1}_{[0,\theta_1]}(\theta_{m,n}) \cos\theta_{m,n}}{\|\mathbf{r}'_m - \mathbf{r}_n\|} k_n\left(t - \frac{\|\mathbf{r}'_m - \mathbf{r}_n\|}{c}\right), m = 1,2,\dots,M, t \geq 0.$$

Accordingly, an element at the m_1-th row and m_2-th column in $\mathbf{H}^{\mathrm{T}}\mathbf{H}$ is expressed in temporally continuous form as

$$\begin{aligned}
&\int_0^{+\infty} s_{m_1}(t) s_{m_2}(t)\mathrm{d}t \\
&= \int_0^{+\infty} \left(\sum_{n=1}^{N} \frac{\mathbf{1}_{[0,\theta_1]}(\theta_{m_1,n}) \cos\theta_{m_1,n}}{\|\mathbf{r}'_{m_1} - \mathbf{r}_n\|} k_n\left(t - \frac{\|\mathbf{r}'_{m_1} - \mathbf{r}_n\|}{c}\right)\right)\left(\sum_{n=1}^{N} \frac{\mathbf{1}_{[0,\theta_1]}(\theta_{m_2,n}) \cos\theta_{m_2,n}}{\|\mathbf{r}'_{m_2} - \mathbf{r}_n\|} k_n\left(t - \frac{\|\mathbf{r}'_{m_2} - \mathbf{r}_n\|}{c}\right)\right)\mathrm{d}t \\
&= \sum_{n_1,n_2 \in \{1,2,\dots,N\}} \frac{\mathbf{1}_{[0,\theta_1]}(\theta_{m_1,n_1}) \cos\theta_{m_1,n_1}}{\|\mathbf{r}'_{m_1} - \mathbf{r}_{n_1}\|} \frac{\mathbf{1}_{[0,\theta_1]}(\theta_{m_2,n_2}) \cos\theta_{m_2,n_2}}{\|\mathbf{r}'_{m_2} - \mathbf{r}_{n_2}\|} \\
&\times \int_{\max\left\{0, \frac{\|\mathbf{r}'_{m_2} - \mathbf{r}_{n_2}\|}{c} - \frac{\|\mathbf{r}'_{m_1} - \mathbf{r}_{n_1}\|}{c}\right\}}^{+\infty} k_{n_1}(t) k_{n_2}\left(t + \frac{\|\mathbf{r}'_{m_1} - \mathbf{r}_{n_1}\|}{c} - \frac{\|\mathbf{r}'_{m_2} - \mathbf{r}_{n_2}\|}{c}\right)\mathrm{d}t \\
&= \sum_{n_1,n_2 \in \{1,2,\dots,N\}} \alpha\left(\mathbf{r}'_{m_1}, \mathbf{r}'_{m_2}, \mathbf{r}_{n_1}, \mathbf{r}_{n_2}\right)\left(k_{n_1} \star k_{n_2}\right)\left(\frac{\|\mathbf{r}'_{m_1} - \mathbf{r}_{n_1}\|}{c} - \frac{\|\mathbf{r}'_{m_2} - \mathbf{r}_{n_2}\|}{c}\right), \\
&\qquad m_1, m_2 \in \{1,2,\dots,M\}.
\end{aligned}$$

Here, we define a weighting factor

$$\alpha\left(\mathbf{r}'_{m_1}, \mathbf{r}'_{m_2}, \mathbf{r}_{n_1}, \mathbf{r}_{n_2}\right) = \frac{\mathbf{1}_{[0,\theta_1]}(\theta_{m_1,n_1}) \cos\theta_{m_1,n_1}}{\|\mathbf{r}'_{m_1} - \mathbf{r}_{n_1}\|} \frac{\mathbf{1}_{[0,\theta_1]}(\theta_{m_2,n_2}) \cos\theta_{m_2,n_2}}{\|\mathbf{r}'_{m_2} - \mathbf{r}_{n_2}\|},$$
$$m_1, m_2 \in \{1,2,\dots,M\}, n_1, n_2 \in \{1,2,\dots,N\}$$

and a cross-correlation function

$$\left(k_{n_1} \star k_{n_2}\right)(\tau) = \int_{\max\{0,-\tau\}}^{+\infty} k_{n_1}(t) k_{n_2}(t+\tau)\mathrm{d}t, \tau \in \mathbb{R}, n_1, n_2 \in \{1,2,\dots,N\}.$$

For any non-zero response $s_m(t)$, we have $\left|\int_0^{+\infty} s_m(t) s_m(t)\mathrm{d}t\right| > 0$. A practical imaging system requires $\left|\int_0^{+\infty} s_{m_1}(t) s_{m_2}(t)\mathrm{d}t\right|$ to be small for any $m_1 \neq m_2$. The image resolution is determined by the decay speed of $\left|\int_0^{+\infty} s_{m_1}(t) s_{m_2}(t)\mathrm{d}t\right|$ as (m_1, m_2) moves away from the diagonal of $\mathbf{H}^{\mathrm{T}}\mathbf{H}$.

To explain the anisotropy of the resolution at $\mathbf{r}'_{m_1}$, we fix m_1 and vary m_2 so that $\mathbf{r}'_{m_2}$ moves from $\mathbf{r}'_{m_1}$ to other locations around $\mathbf{r}'_{m_1}$. Meanwhile, we estimate the decay of $\left|\int_0^{+\infty} s_{m_1}(t) s_{m_2}(t)\mathrm{d}t\right|$. We confine the movement of $\mathbf{r}'_{m_2}$ in a small region around $\mathbf{r}'_{m_1}$ such that the change of $\alpha\left(\mathbf{r}'_{m_1}, \mathbf{r}'_{m_2}, \mathbf{r}_{n_1}, \mathbf{r}_{n_2}\right)$ is negligible. Thus, we only need to elaborate on the decay of $\left|\left(k_{n_1} \star k_{n_2}\right)\left(\frac{\|\mathbf{r}'_{m_1} - \mathbf{r}_{n_1}\|}{c} - \frac{\|\mathbf{r}'_{m_2} - \mathbf{r}_{n_2}\|}{c}\right)\right|$.

We first discuss two special cases: the maximum-cross-correlation matrix

$$\mathrm{MCC}_{n_1,n_2} = \max_{\tau \in \mathbb{R}} \left|\left(k_{n_1} \star k_{n_2}\right)(\tau)\right|, n_1, n_2 \in \{1,2,\dots,N\}$$

and the autocorrelation function $(k_n \star k_n)(\tau), n = 1,2,\dots,N$. Both functions are determined by the bandwidth of the transducer and the configuration of the ER. Here, we performed calibrations at $N = 80 \times 80$ pixels with a spacing of 0.1 mm in each dimension. We pick two locations $\mathbf{r}_{\bar{n}_1}$ and $\mathbf{r}_{\bar{n}_2}$ and calculate the values of $\mathrm{MCC}_{\bar{n}_1,n}$, $\mathrm{MCC}_{\bar{n}_2,n}$, $\left(k_{\bar{n}_1} \star k_{\bar{n}_1}\right)(\tau)$, and $\left(k_{\bar{n}_2} \star k_{\bar{n}_2}\right)(\tau)$. The values of $\mathrm{MCC}_{\bar{n}_1,n}$ and $\mathrm{MCC}_{\bar{n}_2,n}$ for different n form two images shown in **Supplementary Fig. 13a** and **b**, respectively. In each image, we draw two perpendicular lines L_1 and L_2 centered at the corresponding calibration location and compare the pixel values along the lines with the autocorrelation function values (*AC*) expressed as $\left(k_{\bar{n}_1} \star k_{\bar{n}_1}\right)\left(\frac{x}{c}\right)$ or $\left(k_{\bar{n}_2} \star k_{\bar{n}_2}\right)\left(\frac{x}{c}\right)$, as shown in **Supplementary Fig. 13c** and **d**, respectively. As a generalization of the full width at half maximum (FWHM), we define $\mathrm{FW}_{F,\beta}$ as the full width at β times the maximum of a line profile F,

and $\mathrm{FW}_{F,\frac{1}{2}}$ is equivalent to the FWHM of F. For the first selected calibration location $\mathbf{r}_{\bar{n}_1}$, the decay of $\left(k_{\bar{n}_1} \star k_{\bar{n}_1}\right)\left(\frac{x}{c}\right)$ vs. x and the decay of $\mathrm{MCC}_{\bar{n}_1,n}$ vs. $\left|\mathbf{r}_{\bar{n}_1} - \mathbf{r}_n\right|$ are shown in the plots *AC* and L_1-L_2, respectively, in **Supplementary Fig. 13c**. We calculated $\mathrm{FW}_{AC,\beta}$, $\mathrm{FW}_{L_1,\beta}$, and $\mathrm{FW}_{L_2,\beta}$ for β = 0.20 and 0.40. The values are shown in **Supplementary Fig. 13c**. We repeat the quantification for the second selected location $\mathbf{r}_{\bar{n}_2}$, as shown in **Supplementary Fig. 13d**. We observe that the increase of either $\left|\frac{\|\mathbf{r}'_{m_1}-\mathbf{r}_{n_1}\|}{c} - \frac{\|\mathbf{r}'_{m_2}-\mathbf{r}_{n_2}\|}{c}\right|$ or $\left|\mathbf{r}_{n_1} - \mathbf{r}_{n_2}\right|$ causes $\left|\left(k_{n_1} \star k_{n_2}\right)\left(\frac{\|\mathbf{r}'_{m_1}-\mathbf{r}_{n_1}\|}{c} - \frac{\|\mathbf{r}'_{m_2}-\mathbf{r}_{n_2}\|}{c}\right)\right|$ to decay. Equivalently, avoiding the decay of $\left|\left(k_{n_1} \star k_{n_2}\right)\left(\frac{\|\mathbf{r}'_{m_1}-\mathbf{r}_{n_1}\|}{c} - \frac{\|\mathbf{r}'_{m_2}-\mathbf{r}_{n_2}\|}{c}\right)\right|$ requires both $\left|\frac{\|\mathbf{r}'_{m_1}-\mathbf{r}_{n_1}\|}{c} - \frac{\|\mathbf{r}'_{m_2}-\mathbf{r}_{n_2}\|}{c}\right|$ and $\left|\mathbf{r}_{n_1} - \mathbf{r}_{n_2}\right|$ to be small.

Next, we analyze how the probability of both $\left|\frac{\|\mathbf{r}'_{m_1}-\mathbf{r}_{n_1}\|}{c} - \frac{\|\mathbf{r}'_{m_2}-\mathbf{r}_{n_2}\|}{c}\right|$ and $\left|\mathbf{r}_{n_1} - \mathbf{r}_{n_2}\right|$ being small decreases as $\mathbf{r}'_{m_2}$ moves away from $\mathbf{r}'_{m_1}$. We only discuss two representative cases: (1) $\mathbf{r}'_{m_2}$ moves on the plane crossing $\mathbf{r}'_{m_1}$ and parallel to the calibration plane (**Supplementary Fig. 13e** and **f**); (2) $\mathbf{r}'_{m_2}$ moves on the line crossing $\mathbf{r}'_{m_1}$ and normal to the calibration plane (**Supplementary Fig. 13g** and **h**). In the first case, we let $\frac{\|\mathbf{r}'_{m_1}-\mathbf{r}_{n_1}\|}{c} = \frac{\|\mathbf{r}'_{m_2}-\mathbf{r}_{n_2}\|}{c}$ and observe how the probability of $\left|\mathbf{r}_{n_1} - \mathbf{r}_{n_2}\right|$ being small is violated. Because $\frac{\|\mathbf{r}'_{m_1}-\mathbf{r}_{n_1}\|}{c} = \frac{\|\mathbf{r}'_{m_2}-\mathbf{r}_{n_2}\|}{c}$ and locations $\mathbf{r}'_{m_1}$ and $\mathbf{r}'_{m_2}$ are with the same distance to the calibration plane, locations $\mathbf{r}_{n_1}$ and $\mathbf{r}_{n_2}$ must be on two circles with the same radius and their centers separated by $\left|\mathbf{r}'_{m_1} - \mathbf{r}'_{m_2}\right|$. If $\left|\mathbf{r}'_{m_1} - \mathbf{r}'_{m_2}\right|$ is small, for any $\mathbf{r}_{n_1}$ on one circle, there exists a $\mathbf{r}_{n_2}$ on the other circle such that $\left|\mathbf{r}_{n_1} - \mathbf{r}_{n_2}\right|$ is small, as shown in **Supplementary Fig. 13e**. If $\left|\mathbf{r}'_{m_1} - \mathbf{r}'_{m_2}\right|$ is large, a small value of $\left|\mathbf{r}_{n_1} - \mathbf{r}_{n_2}\right|$ requires both $\mathbf{r}_{n_1}$ and $\mathbf{r}_{n_2}$ to be close to the same intersection of the two circles, as depicted in **Supplementary Fig. 13f**. Thus, the higher the value of $\left|\mathbf{r}'_{m_1} - \mathbf{r}'_{m_2}\right|$, the lower the probability of $\left|\mathbf{r}_{n_1} - \mathbf{r}_{n_2}\right|$ being small. In summary, for the first case, the decay speed of $\left|\int_0^{+\infty} s_{m_1}(t)s_{m_2}(t)\mathrm{d}t\right|$ as $\left|\mathbf{r}'_{m_1} - \mathbf{r}'_{m_2}\right|$ increases is mainly determined by MCC_{n_1,n_2}'s decay speed as $\left|\mathbf{r}_{n_1} - \mathbf{r}_{n_2}\right|$ increases. In the second case, we let $n_1 = n_2 = n$ and observe the change of $\tau = \left|\frac{\|\mathbf{r}'_{m_1}-\mathbf{r}_n\|}{c} - \frac{\|\mathbf{r}'_{m_2}-\mathbf{r}_n\|}{c}\right|$. As $\mathbf{r}'_{m_2}$ moves away from $\mathbf{r}'_{m_1}$ (from **Supplementary Fig. 13g** to **h**), $c\tau = \left|\mathbf{r}'_{m_1} - \mathbf{r}'_{m_2}\right|\cos\theta$ increases. Here, θ is the angle between vectors $\mathbf{r}_n - \mathbf{r}'_{m_1}$ and $\mathbf{r}'_{m_2} - \mathbf{r}'_{m_1}$. If $\mathbf{r}_n$, $\mathbf{r}'_{m_1}$, and $\mathbf{r}'_{m_2}$ are on the same line, the calibrated virtual transducer at $\mathbf{r}_n$ is the most sensitive to the signals from $\mathbf{r}'_{m_1}$ and $\mathbf{r}'_{m_2}$, and $\cos\theta \approx 1$. Thus, for the second case, the decay of $\left|\int_0^{+\infty} s_{m_1}(t)s_{m_2}(t)\mathrm{d}t\right|$ as $\left|\mathbf{r}'_{m_1} - \mathbf{r}'_{m_2}\right|$ increases is mainly determined by the decay of $\left|\left(k_n \star k_n\right)\left(\frac{|\mathbf{r}'_{m_1}-\mathbf{r}'_{m_2}|}{c}\right)\right|$. We compare the decay speed of MCC_{n_1,n_2} as $\left|\mathbf{r}_{n_1} - \mathbf{r}_{n_2}\right|$ increases and that of $\left|\left(k_n \star k_n\right)\left(\frac{|\mathbf{r}'_{m_1}-\mathbf{r}'_{m_2}|}{c}\right)\right|$ as $\left|\mathbf{r}'_{m_1} - \mathbf{r}'_{m_2}\right|$ increases by observing the full-width values in **Supplementary Fig. 13c** and **d**. For both calibrated virtual transducers and all choices of β, values of $\mathrm{FW}_{L_1,\beta}$ and $\mathrm{FW}_{L_2,\beta}$ are of 4 to 8 times the value of $\mathrm{FW}_{AC,\beta}$.

The substantial decay-speed difference between $\mathrm{FW}_{L_1,\beta}$ or $\mathrm{FW}_{L_2,\beta}$ with $\mathrm{FW}_{AC,\beta}$ leads to the anisotropy of $\left|\int_0^{+\infty} s_{m_1}(t)s_{m_2}(t)\mathrm{d}t\right|$'s decay speed as $\left|\mathbf{r}'_{m_1} - \mathbf{r}'_{m_2}\right|$ increases, which contributes to the anisotropy of the image resolution. It needs to be noted that, we have simplified the above analysis to identify the cross-correlation-related and autocorrelation-related limiting factors. In practice, the anisotropy is affected by both the maximum-cross-correlation matrix MCC_{n_1,n_2} and the autocorrelation function $(k_n \star k_n)(\tau)$ for all values of n_1, n_2, and n with different weights. These factors are incorporated into the iterative method and lead to the final anisotropy of resolution in the reconstructed image.

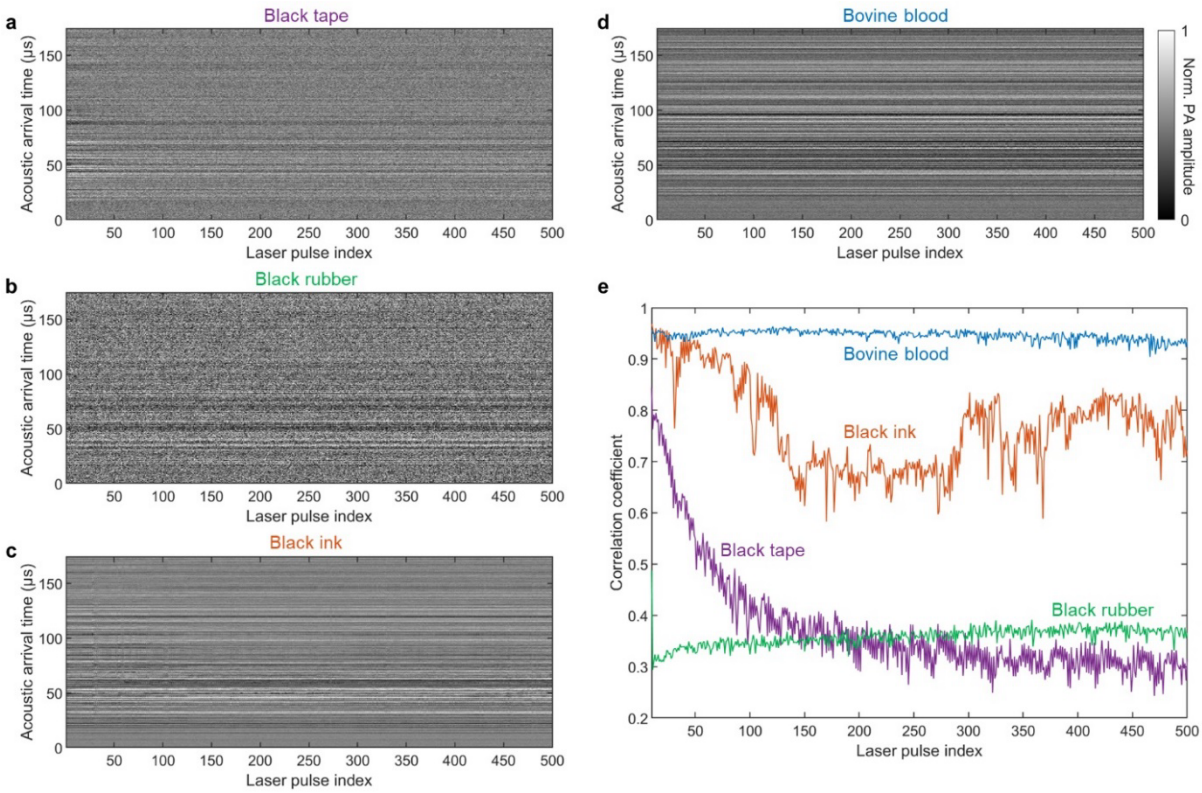

Supplementary Fig. 1 l Comparison of uniform optical absorbers for calibration.
a–d, PACTER signals generated by 500 consecutive laser pulses (8.6 μJ pulse energy, 1 kHz repetition rate) using black tape (**a**), black rubber (**b**), black ink (**c**), and bovine blood (**d**) as targets. Norm., normalized. **e**, Correlation coefficients between the PACTER signals and the average of the signals from the first 10 laser pulses.

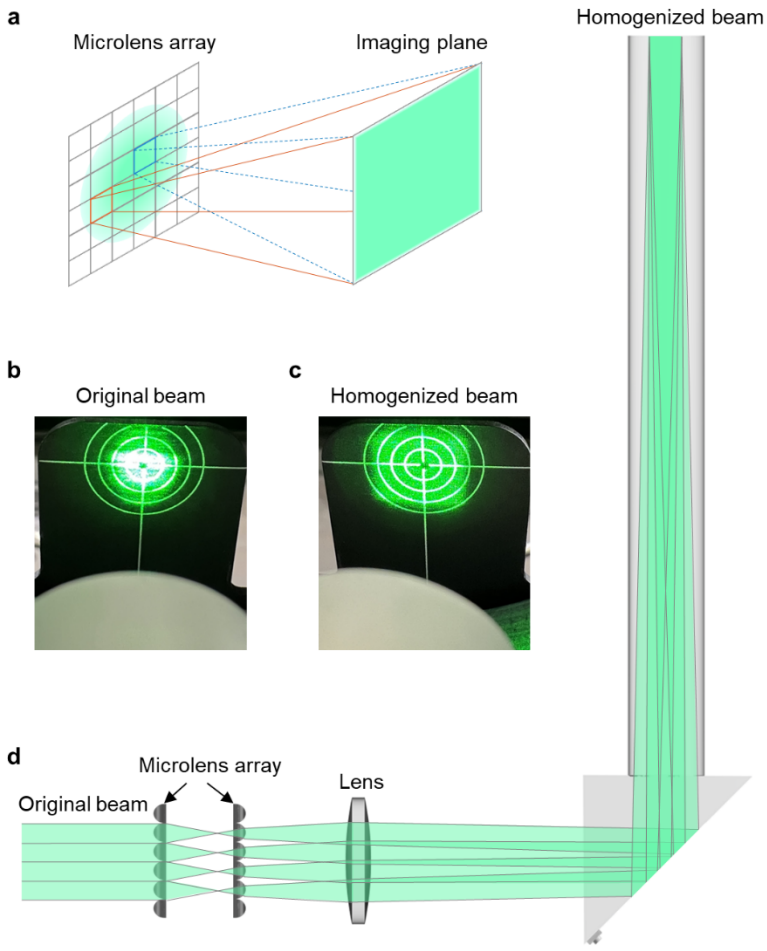

Supplementary Fig. 2 | Fly's eye homogenizer in PACTER.
a, Schematic illustrating the working principle of the fly's eye homogenizer. **b,c**, Photographs of the original beam from the laser (**b**) and the homogenized beam (**c**), captured using a laser alignment plate 1 cm away from the top of the ER. **d**, Schematic showing the optical path of the homogenizer and the ER.

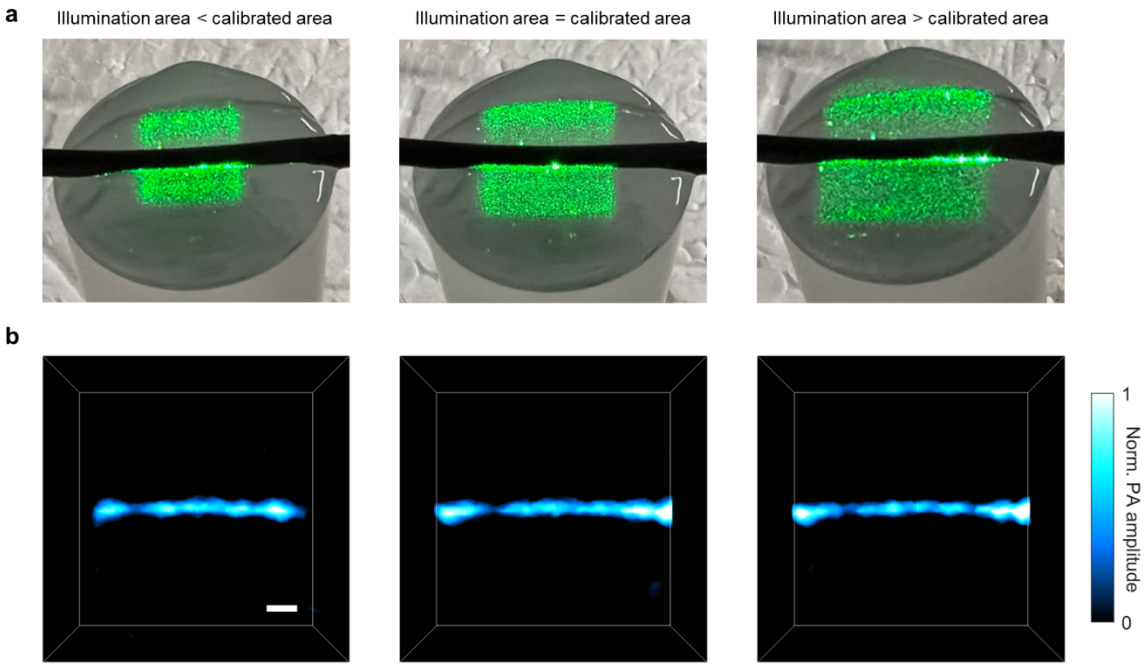

Supplementary Fig. 3 | PACTER with different illumination areas.
a, Photographs showing PACTER imaging experiments when the illumination area is smaller (left), equivalent (middle), and larger (right) compared with the calibrated area. **b**, Perspective views of 3D PACTER images of the black wire in **a**, acquired when the illumination area is smaller (left), equivalent (middle), and larger (right) compared with the calibrated area. Norm., normalized. Scale bar, 1 mm.

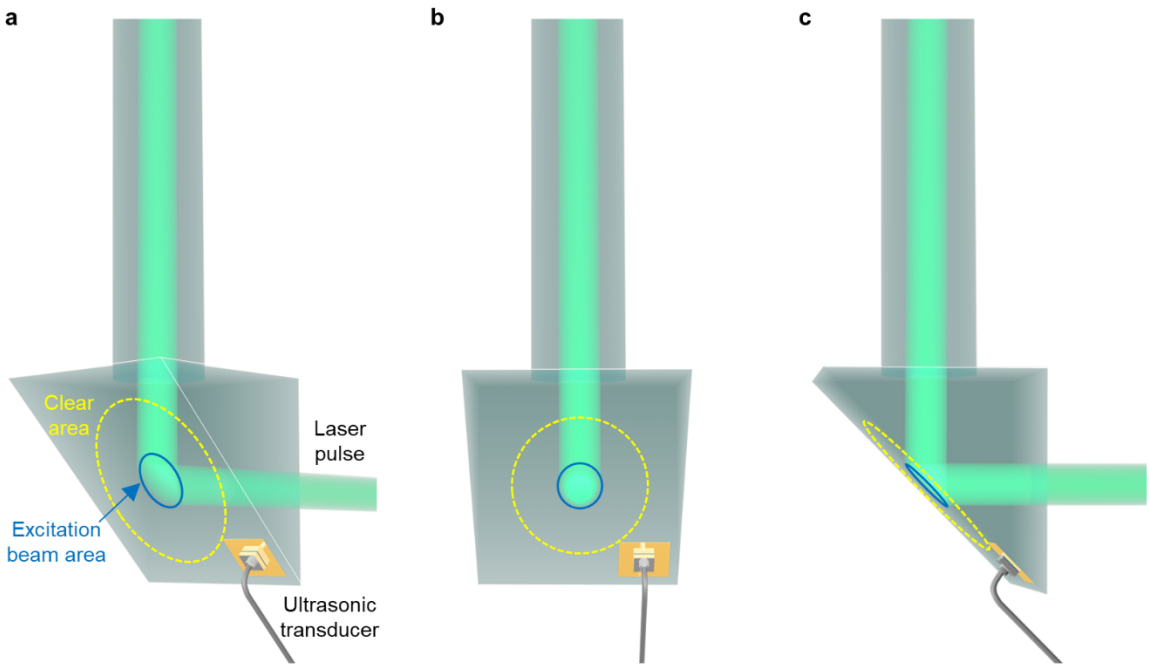

Supplementary Fig. 4 l Positioning of the single-element ultrasonic transducer on the ER. **a–c**, ER, excitation laser beam, and single-element ultrasonic transducer viewed at different angles. The blue solid circle indicates the area of the excitation beam on the hypotenuse surface of the prism of the ER. The yellow dashed circle indicates a clear area, where the laser beam does not interact with the ultrasonic transducer.

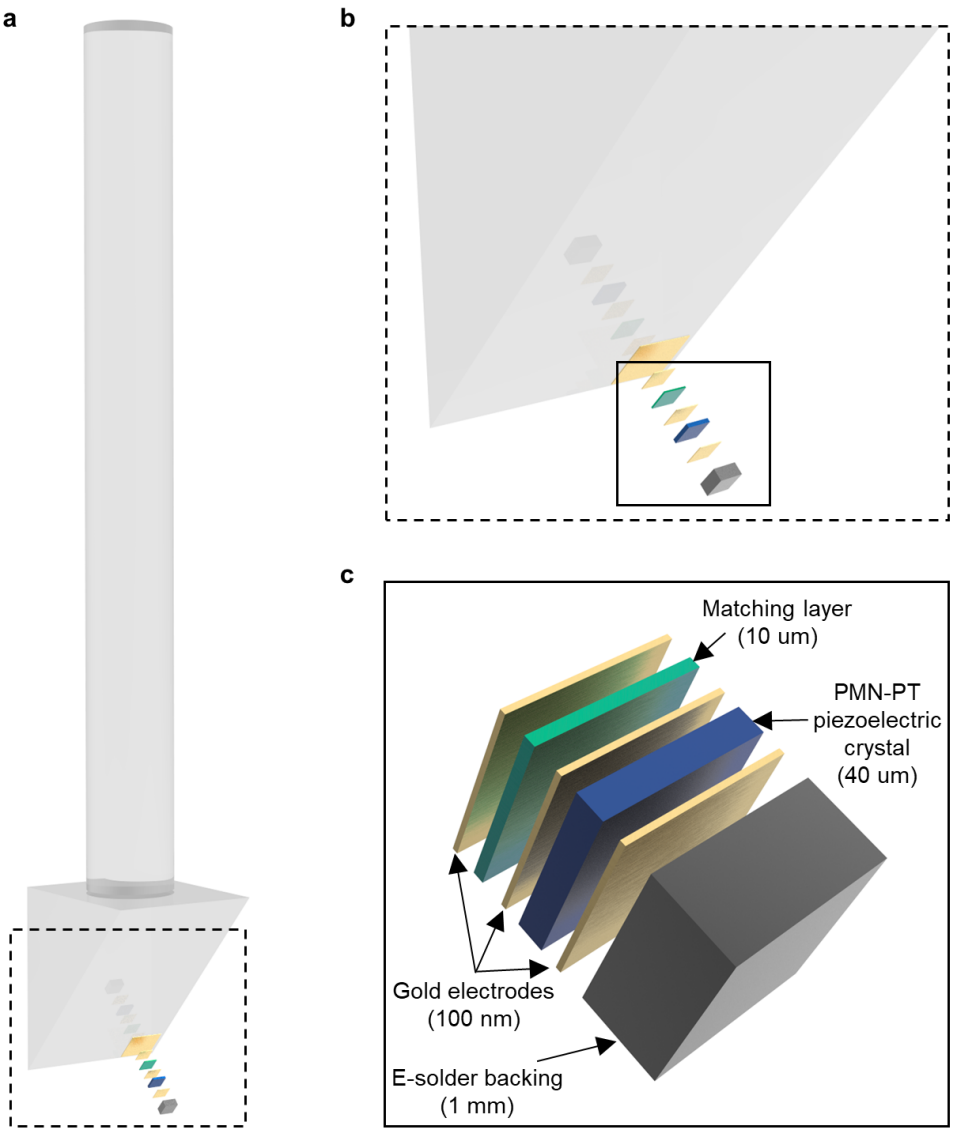

Supplementary Fig. 5 l Fabrication of the single-element ultrasonic transducer.
a, Schematic showing the ultrasonic transducer fabricated on the ER. **b**, Zoomed-in view of the black dashed box in **a**. **c**, Zoomed-in view of the black solid box in **b**. Thicknesses of different layers of materials are provided in brackets.

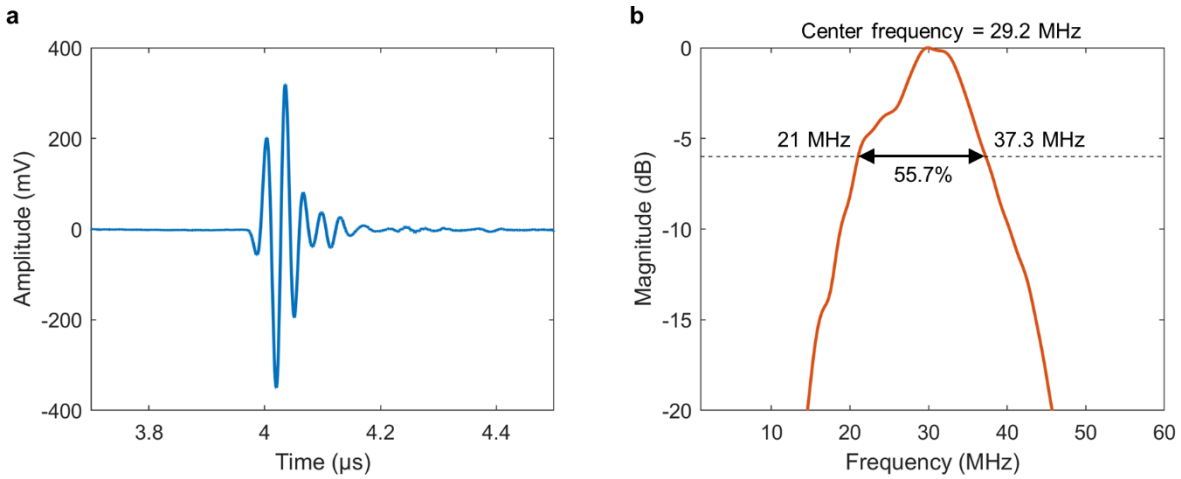

Supplementary Fig. 6 | Characterization of the single-element ultrasonic transducer. Pulse-echo waveform (**a**) and -6 dB bandwidth (**b**) of the fabricated ultrasonic transducer measured before being glued to the ER.

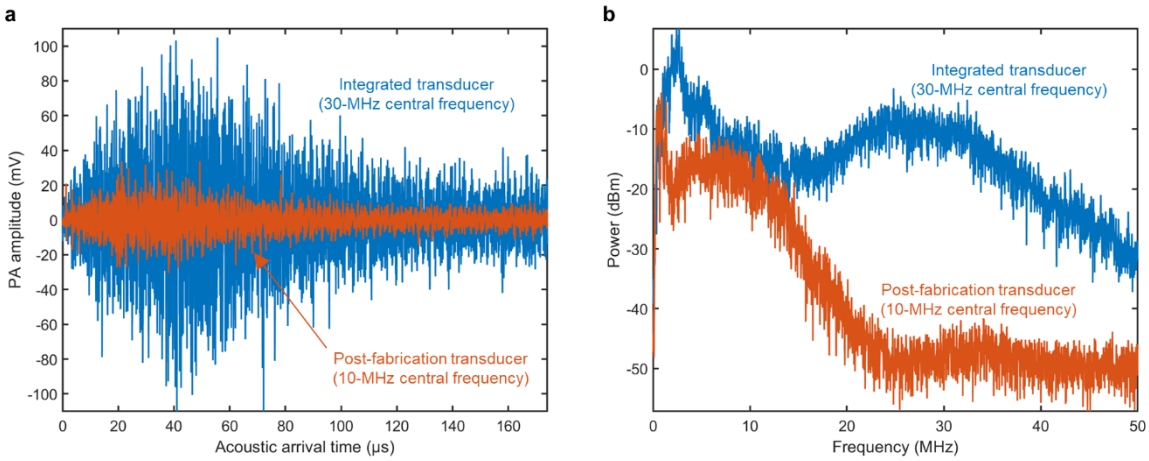

Supplementary Fig. 7 | Comparison of the integrated and post-fabrication transducers.
a, PA signals detected by the integrated PMN-PT transducer fabricated on the ER (blue) and the post-fabrication transducer (XMS-310, Olympus Corporation) coupled to the ER with resin (orange) in PACTER. **b**, Spectra of the PA signals in **a**.

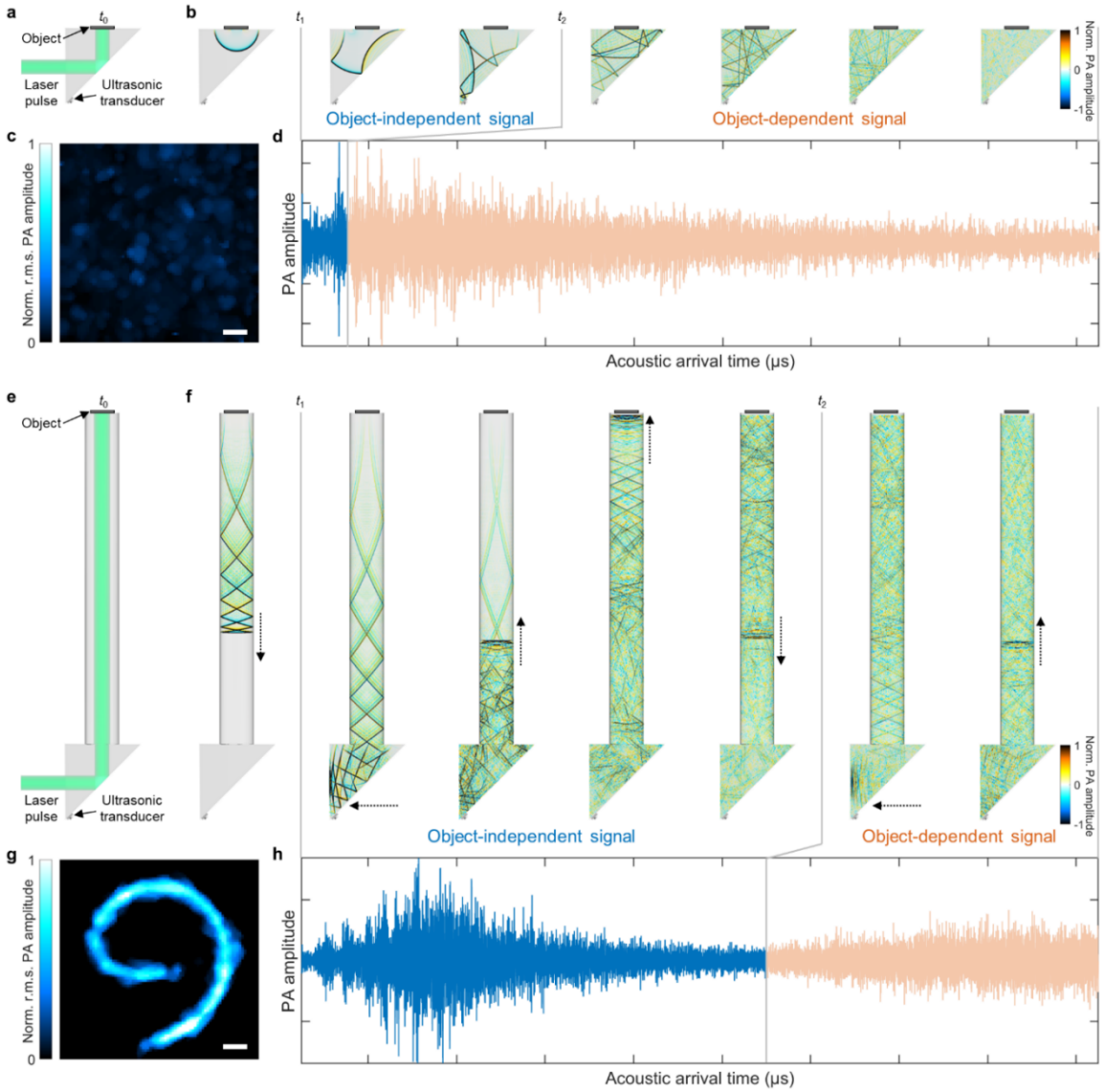

Supplementary Fig. 8 | Object-dependent and -independent calibrations in PATER and PACTER, respectively.
a, Optical path of the ER in PATER. t_0 denotes the time instance of laser pulse illumination. **b**, Time-lapse simulation of the PA signal propagating in the ER in PATER. t_1 denotes the time instance when the transducer starts to detect the PA signal. t_2 denotes the time instance when the transducer starts to detect the object-dependent PA signal, which is reflected from the object and affected by the boundary condition. Norm., normalized. **c**, Reconstructed image of a black wire using the ER in PATER calibrated with bovine blood, showing the object dependence of calibration. **d**, PA signal detected by a transducer attached to the ER in PATER. **e**, Optical path of the ER in PACTER. **f**, Time-lapse simulation of the PA signal propagating in the ER in PACTER. Black dotted arrows denote the propagating direction of the acoustic wavefront. The definitions of t_0, t_1, t_2 are identical to those in **a** and **b**. **g**, Reconstructed image of a black wire using the ER in PACTER calibrated with bovine blood, showing the object independence or universality of calibration. **h**, PA signal detected by the transducer fabricated on the ER in PACTER. Object-independent and -dependent signal segments are color-coded in blue and light orange, respectively. Scale bars, 1 mm.

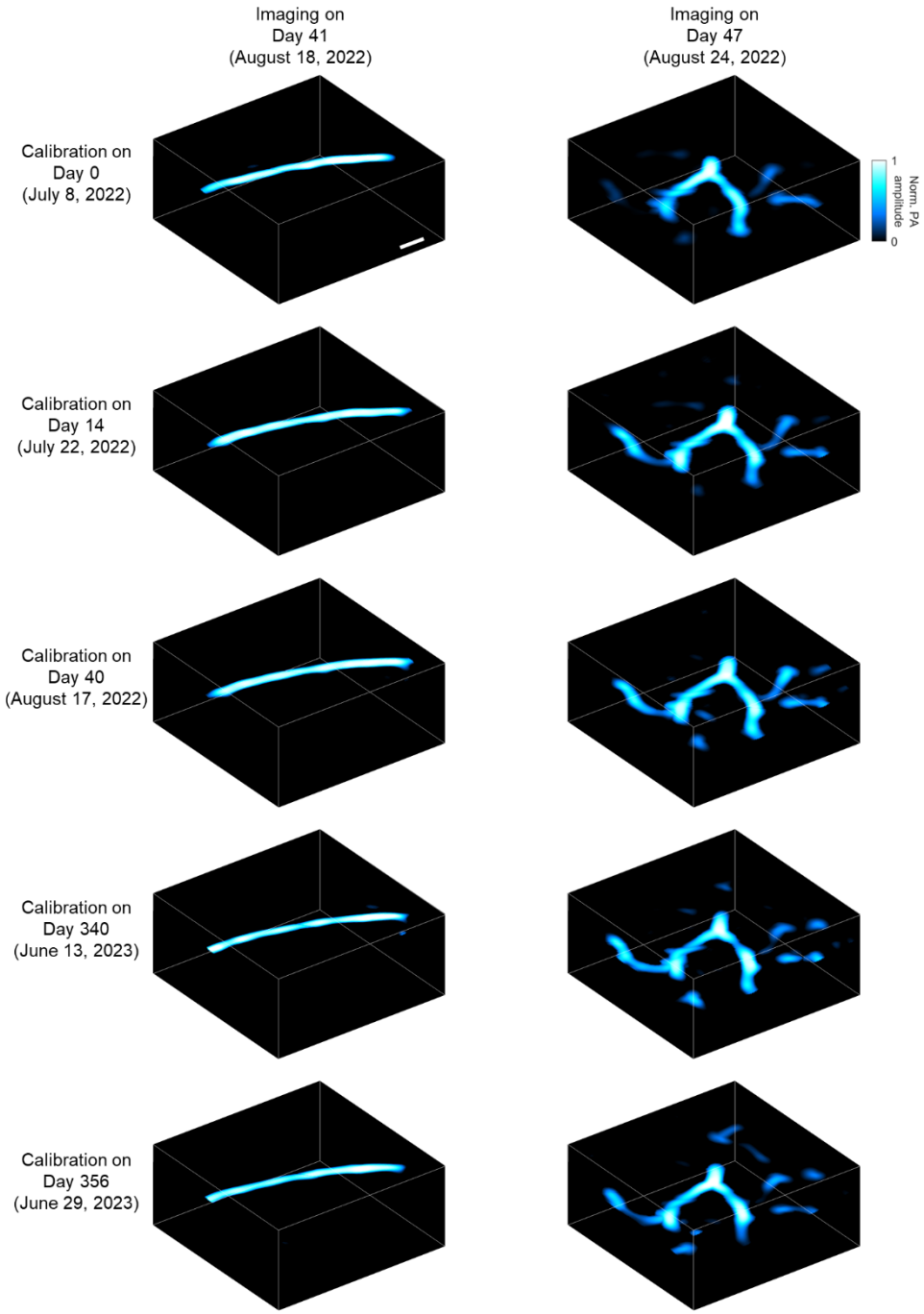

Supplementary Fig. 9 | PACTER reconstruction using the calibration data acquired at different times. Denoting July 8, 2022 as Day 0, the calibration data were acquired on Days 0, 14, 40, 340, and 356. All of them can be used to reconstruct the imaging data acquired on Days 41 and 47, which were acquired from a tube filled with bovine blood and the thenar vasculature of participant 1, respectively. Norm., normalized. Scale bar, 1 mm.

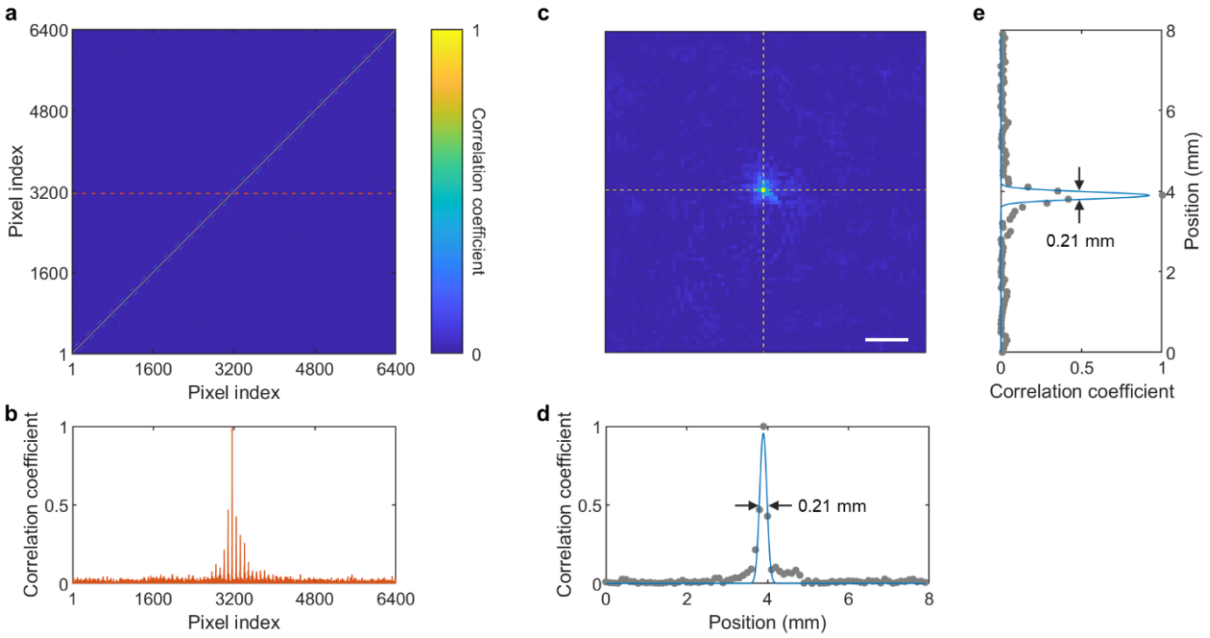

Supplementary Fig. 10 l PACTER signals from calibration using bovine blood.
a, Cross-correlation map of the PACTER signals from the calibration pixels (80 by 80 steps with a 0.1 mm step size), where the diagonal line represents autocorrelation. **b**, Line profile along the orange dashed line in **a**. **c**, Cross-correlation map (80 by 80 pixels) reshaped from the cross-correlation profile in **b**. Scale bar, 1 mm. **d**,**e**, Line profiles along the horizontal (**d**) and vertical (**e**) yellow dashed lines in **c**. Both FWHMs of the fitted profiles are ~0.21 mm.

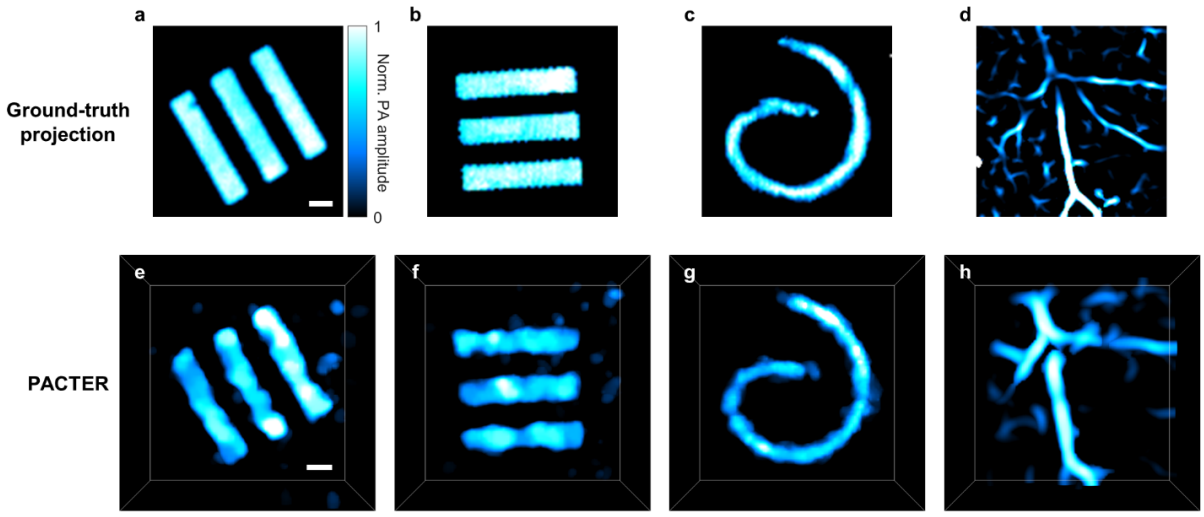

Supplementary Fig. 11 | Validation of PACTER reconstruction.
a–d, Ground-truth projection images of the objects: bars printed with black ink on a transparent film (**a,b**), curved black wire (**c**), and mouse abdominal vasculature *in vivo* (**d**). The images were acquired in a way similar to the calibration procedure, except that the bovine blood was replaced by the objects. The images were formed by the root-mean-squared projections of the PACTER signals as the focused laser beam scanned across the objects. Norm., normalized. **e–h**, Perspective views of 3D PACTER images of the objects in **a–d** acquired through the imaging procedure using a homogenized beam. Scale bars, 1 mm.

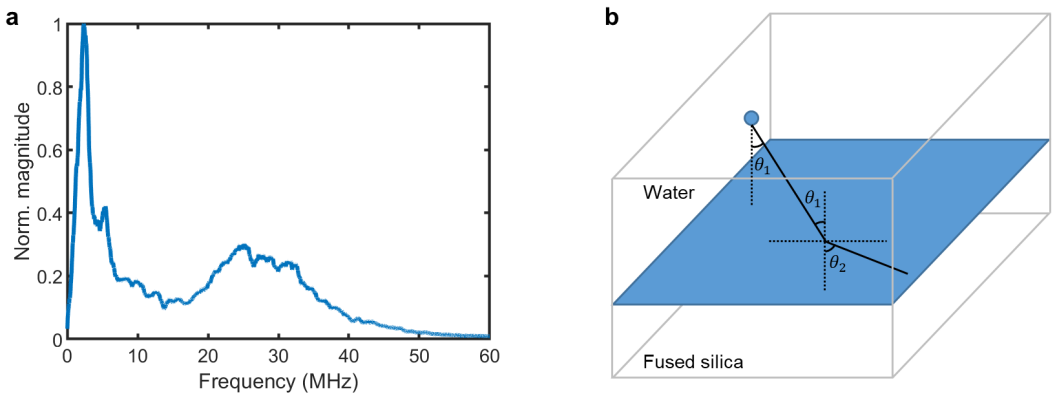

Supplementary Fig. 12 l Spatial resolution analysis from the virtual-transducer-array perspective. **a** Spectrum of the PACTER signal from the phantom shown in **Fig. 3**f. **b** Refraction of the ultrasonic wave at the boundary between water and fused silica. θ_1 is the incident angle. θ_2 is the refraction angle.

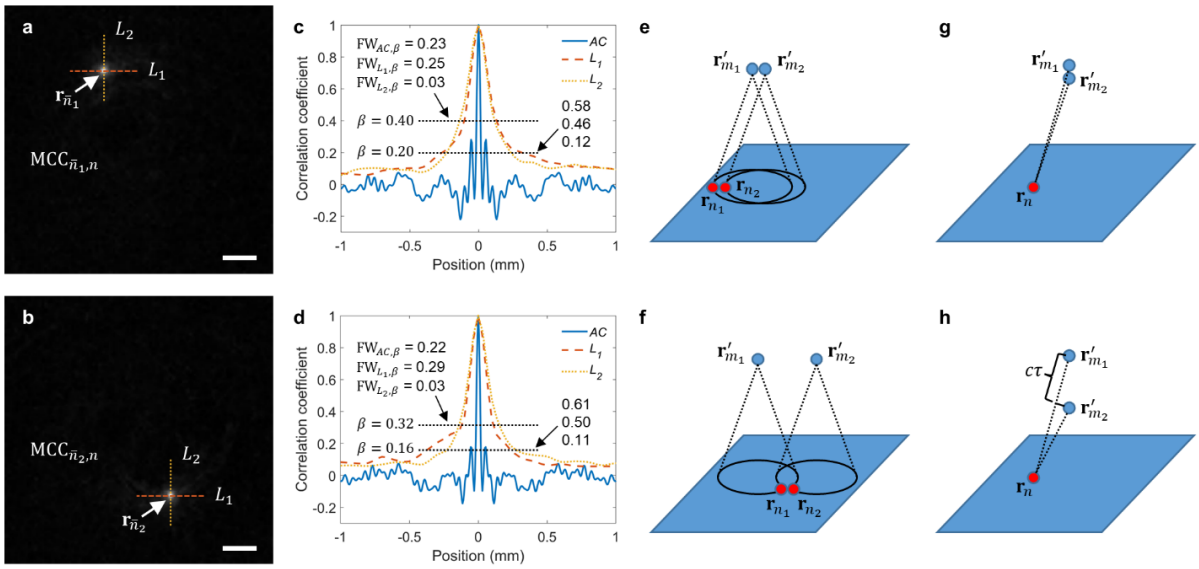

Supplementary Fig. 13 | Spatial resolution analysis from the system-matrix perspective. **a-b**, Two slices of the maximum-cross-correlation matrix ($\mathrm{MCC}_{\bar{n}_1,n}$ and $\mathrm{MCC}_{\bar{n}_2,n}$, each value means the maximum cross correlation between two impulse responses in the calibration) corresponding to the $\bar{n}_1$-th and $\bar{n}_2$-th calibrated virtual transducers, respectively. Two lines L_1 and L_2 are drawn in each image. Scale bars, 1 mm. **c-d**, Maximum-cross-correlation values along lines L_1 and L_2 aligned with the values of $(k_n \star k_n)\left(\frac{x}{c}\right)$ for the $\bar{n}_1$-th and $\bar{n}_2$-th calibrated virtual transducers, respectively. **e-f**, A source point at $\mathbf{r}'_{m_2}$ moves away from another source point at $\mathbf{r}'_{m_1}$ (from **e** to **f**) with both source points on a line parallel to the calibration plane. In each image, we mark two close calibrated virtual transducers $\mathbf{r}_{n_1}$ and $\mathbf{r}_{n_2}$ which satisfy $\frac{\|\mathbf{r}'_{m_1}-\mathbf{r}_{n_1}\|}{c} = \frac{\|\mathbf{r}'_{m_2}-\mathbf{r}_{n_2}\|}{c}$. **g-h**, A source point at $\mathbf{r}'_{m_2}$ moves away from another source point at $\mathbf{r}'_{m_1}$ (from **g** to **h**) with both source points on a line normal to the calibration plane. The same calibrated virtual transducer $\mathbf{r}_n$ is marked in both **g** and **h** with the difference between its distances to $\mathbf{r}'_{m_1}$ and $\mathbf{r}'_{m_2}$ denoted as $c\tau$.

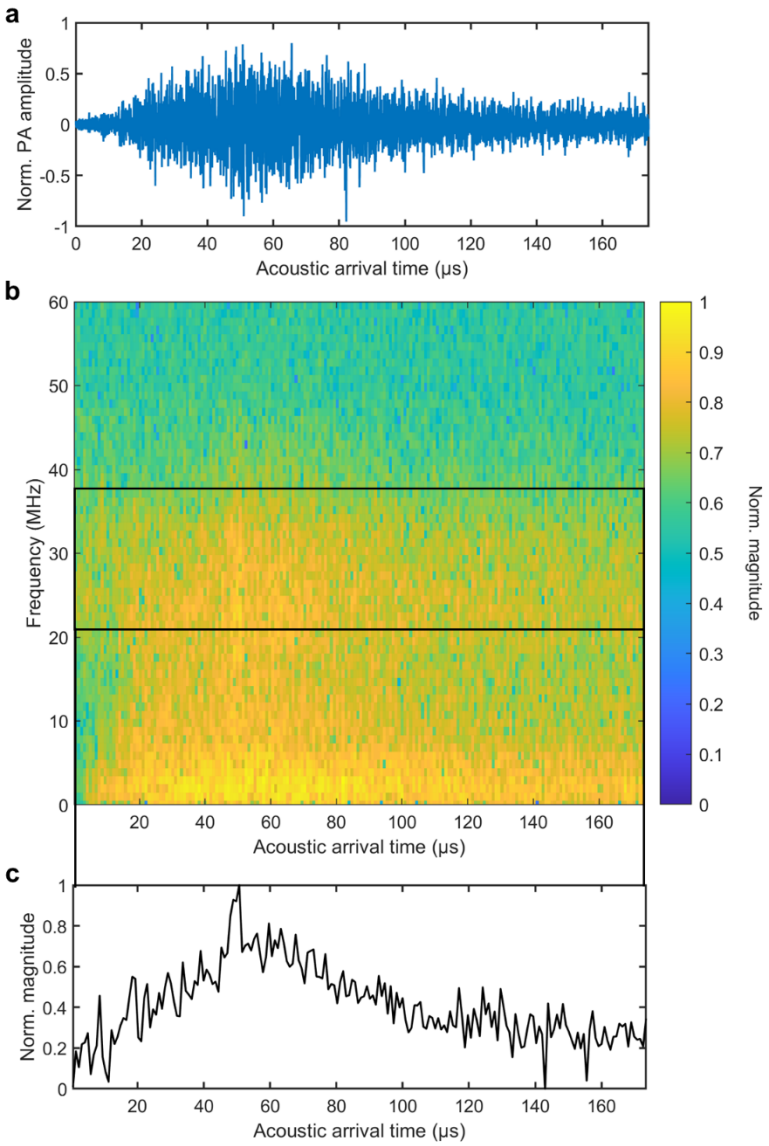

Supplementary Fig. 14 l Spectrogram of the PACTER signal.
a, PACTER signal of bovine blood in the time domain. Norm., normalized. **b**, Spectrogram of the PACTER signal in **a** calculated using a short-time Fourier transformation (256 samples per section, 32 samples overlapped between sections). **c**, Spectral magnitude averaged over the bandwidth of the ultrasonic transducer, i.e., from 21 MHz to 37.3 MHz, versus time, corresponding to the black box in **b**.

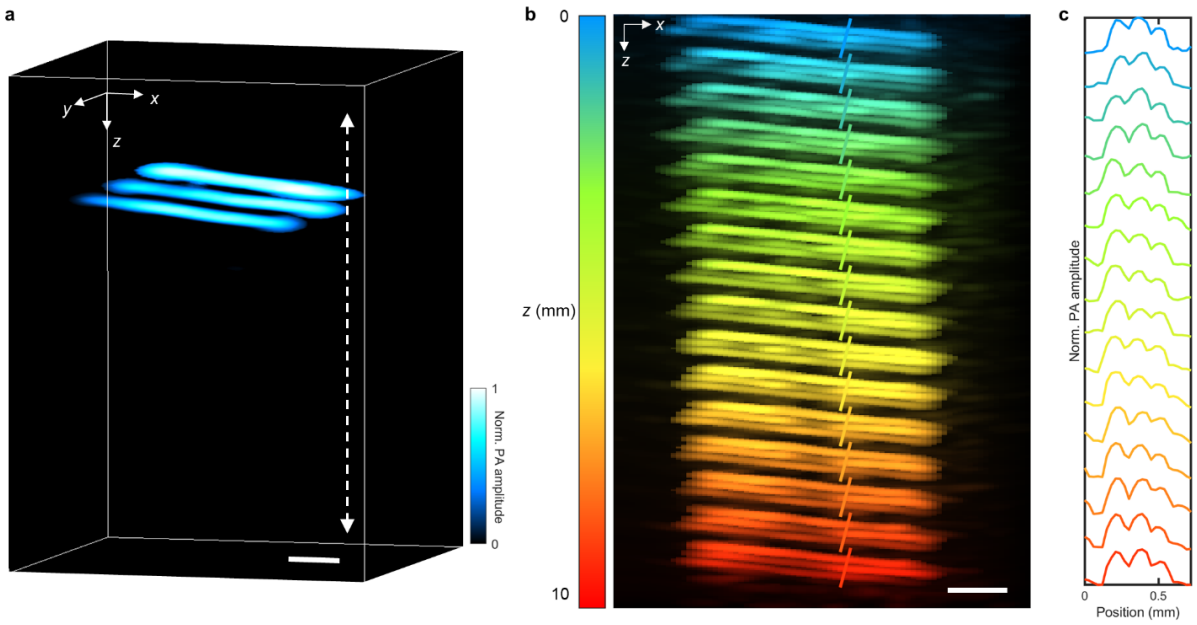

Supplementary Fig. 15 l 3D PACTER images of an object placed at different depths.
a, 3D PACTER image of three bars printed with black ink on a transparent film. The dashed line indicates that the object is translated along the *z*-axis to be imaged at different depths. Norm., normalized. **b**, Summation of the maximum *y*-projections of the 3D volumes like **a** where the object is placed at different depths. The *z*-positions of the object are color-encoded. **c**, Profiles along the solid lines in **b**. The colors represent the depths of the object. Scale bars, 1 mm.

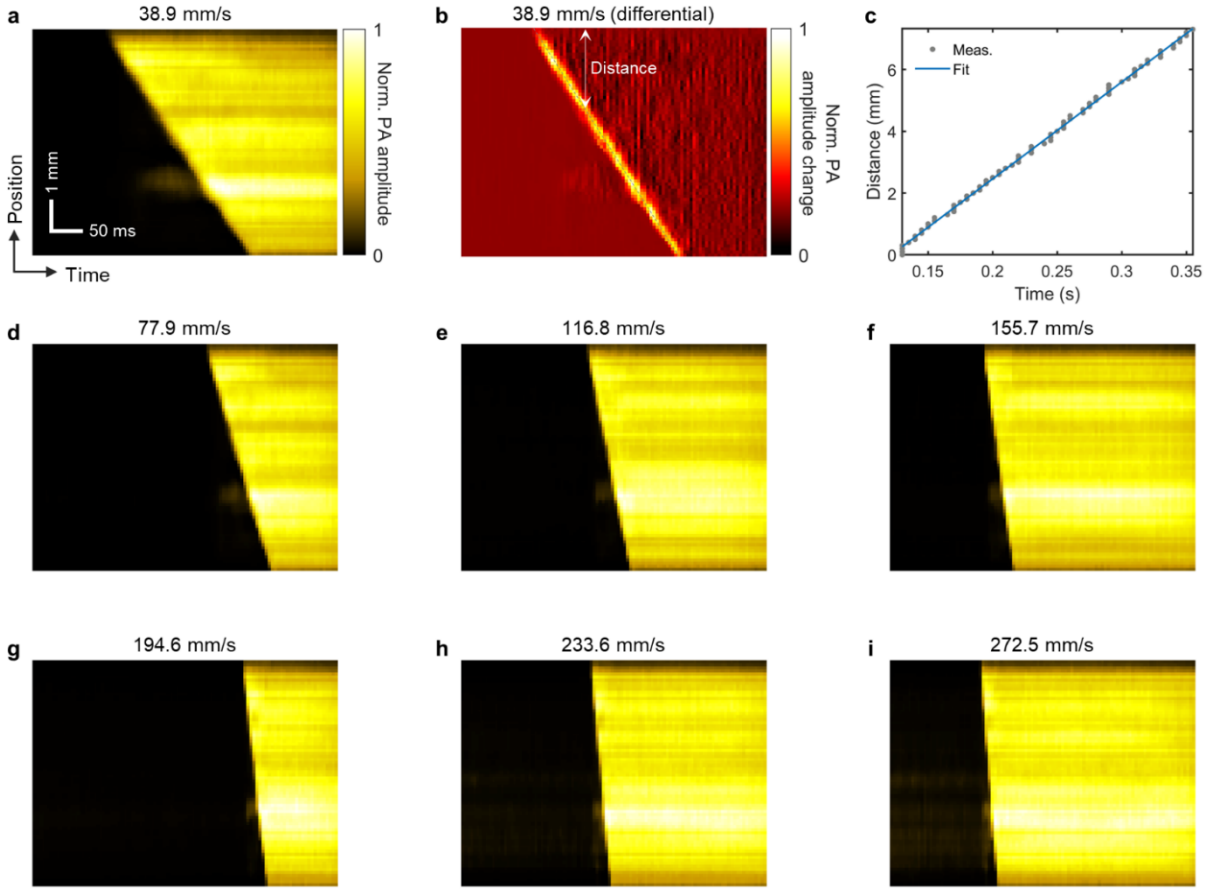

Supplementary Fig. 16 | PACTER of bovine blood flushing through a tube.
a, PA amplitudes along the tube (1D image) flushed by the blood with a speed of 38.9 mm/s versus time. Norm., normalized. **b**, Differential image of **a** (difference between adjacent voxels along the tube in **a** versus time) showing the distance the blood front travels over time. **c**, Traveling distance of the blood front plotted over time. Blue curve represents a linear fit. **d–i**, PA amplitudes along the tube (1D images) flushed by the blood with different speeds versus time.

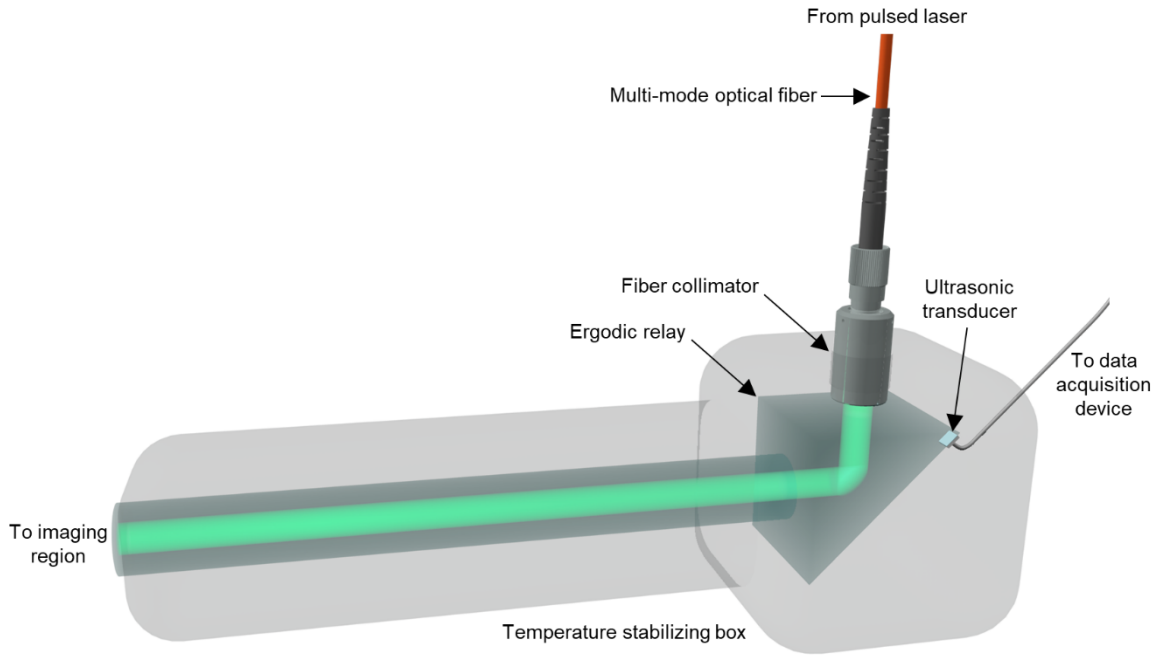

Supplementary Fig. 17 | Schematic of a PACTER system allowing handheld operation.
The PACTER system can be modified by utilizing a multi-mode optical fiber to deliver the excitation light beam, adding flexibility for animal and human imaging.

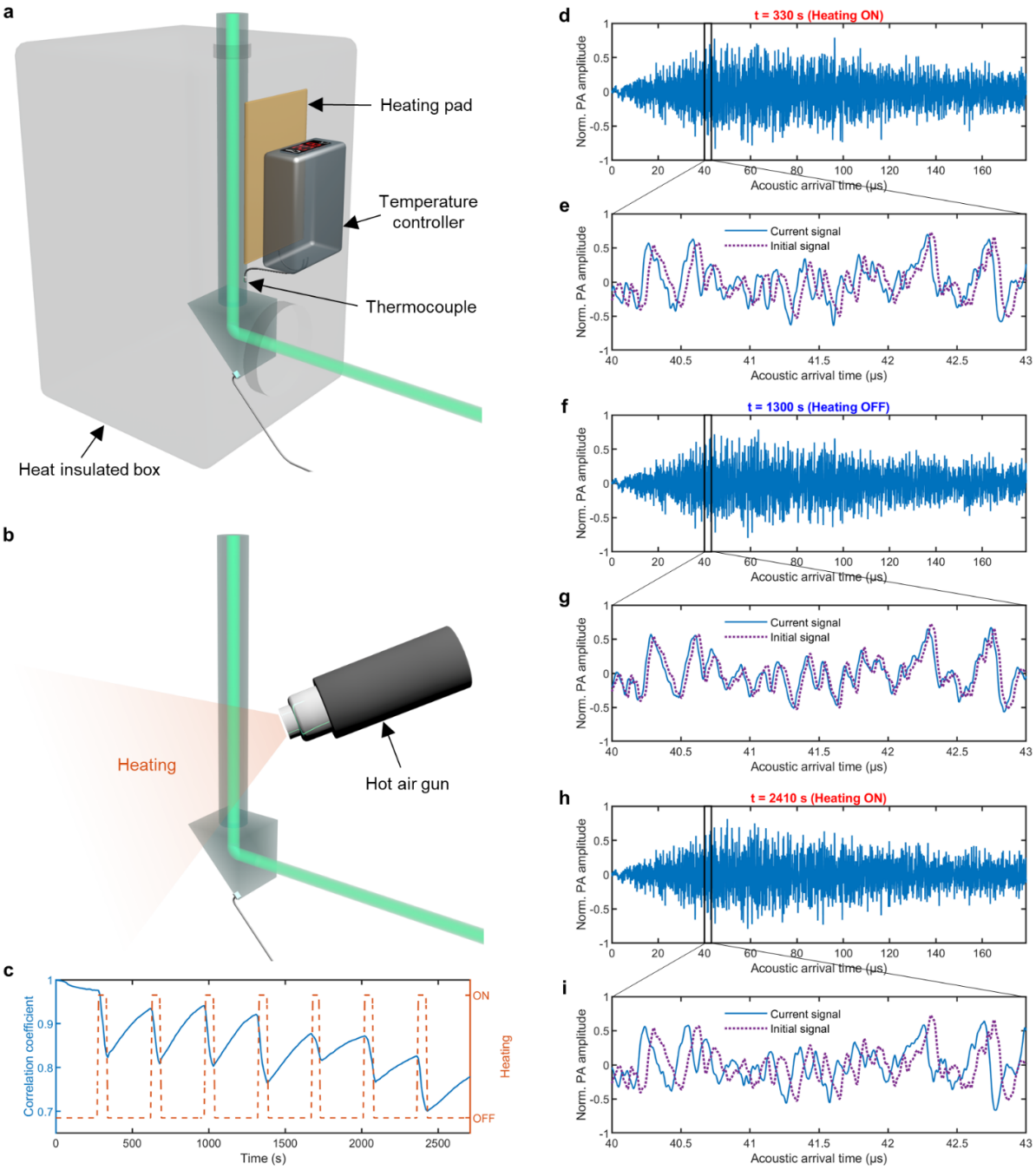

Supplementary Fig. 18 | Temperature stabilization in PACTER.
a, Schematic of the temperature stabilizing box in the PACTER system. **b**, Illustration of the experiment showing the temperature dependence of the PACTER system. During acquisition of PACTER signals, the hot air gun is turned ON and OFF to provide periodic heating to the ER. **c**, Correlation coefficient (blue solid curve) between each PACTER signal and the initial signal acquired using bovine blood, and the ON and OFF status (orange dashed curve) of the hot air gun. **d,f,h**, PACTER signals acquired at 330 s with heating on (**d**), 1300 s with heating off (**f**), and 2410 s with heating on (**h**). Norm., normalized. **e,g,i**, The blue solid lines represent the zoomed-in views of the black boxes in **d** (**e**), **f** (**g**), and **h** (**i**). The purple dotted lines show the initial signal acquired at 0 s.

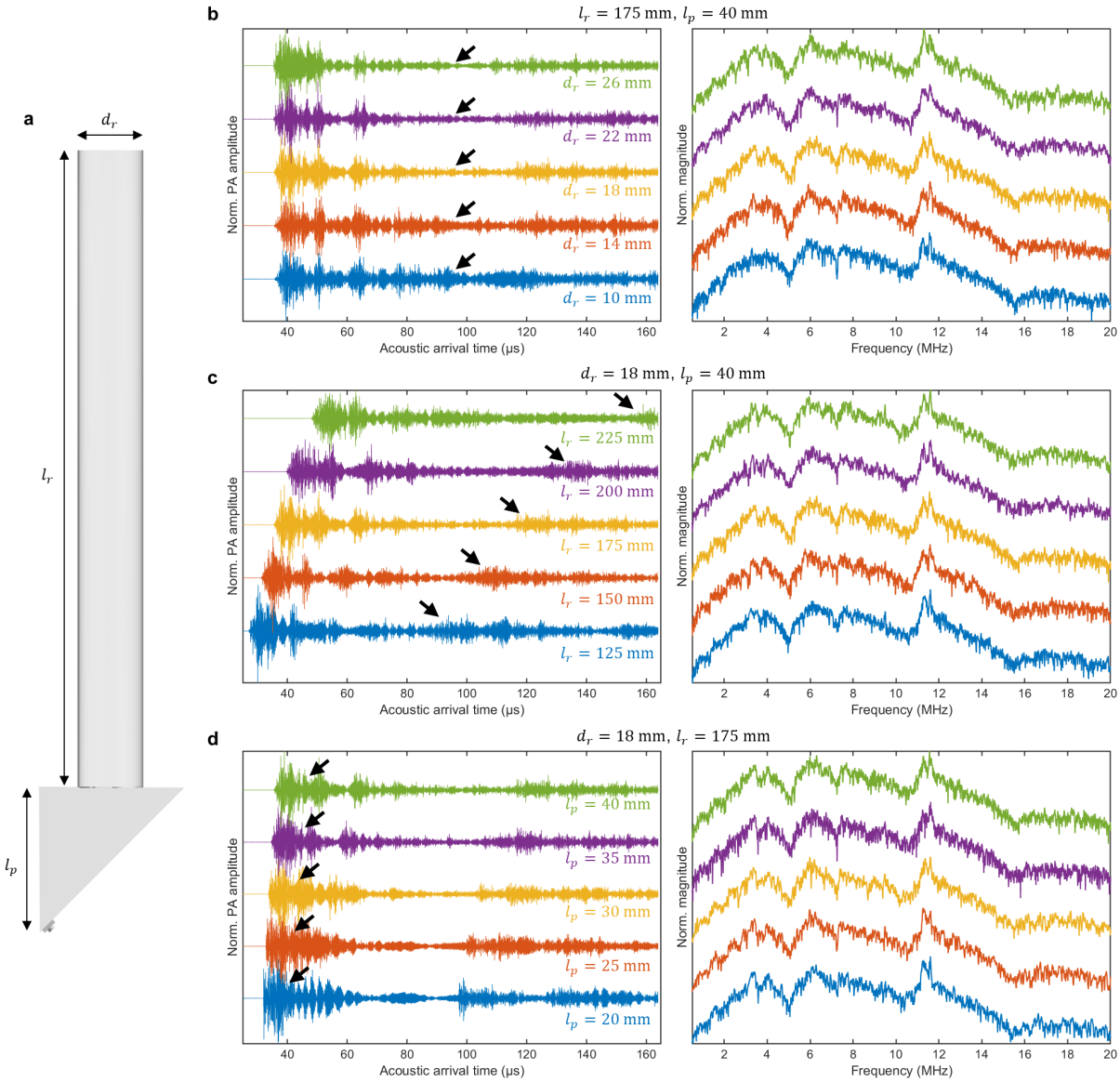

Supplementary Fig. 19 | Simulation of PACTER signals from ERs with different dimensions. **a**, Schematic showing the dimensions of the ER, including the diameter (d_r) and the length (l_r) of the fused silica rod, and the right-angle edge length (l_p) of the prism. **b**, Simulated PACTER signals (left) and their spectra (right) from ERs with different d_r. Black arrows indicate the tails of the scrambled PA signals. **c**, Simulated PACTER signals (left) and their spectra (right) from ERs with different l_r. Black arrows indicate the PA signals reflected from the object. **d**, Simulated PACTER signals (left) and their spectra (right) from ERs with different l_p. Black arrows indicate the PA signals scrambled by the prism. We conducted the simulations using the *k*-wave toolbox. Each simulation took about 11 hours running on an NVIDIA GeForce RTX 3060 GPU. Despite the considerable time requirement, it was impractical for us to use the *k*-wave toolbox to simulate real experimental signals due to the following reasons: (1) the simulations were performed in 2D, while the experiments were conducted in 3D; (2) the maximum frequency supported by the simulations was 8.575 MHz, which is substantially lower compared to the bandwidth of our experimental signals. Thus, these simulations should only be used for qualitative assessments.

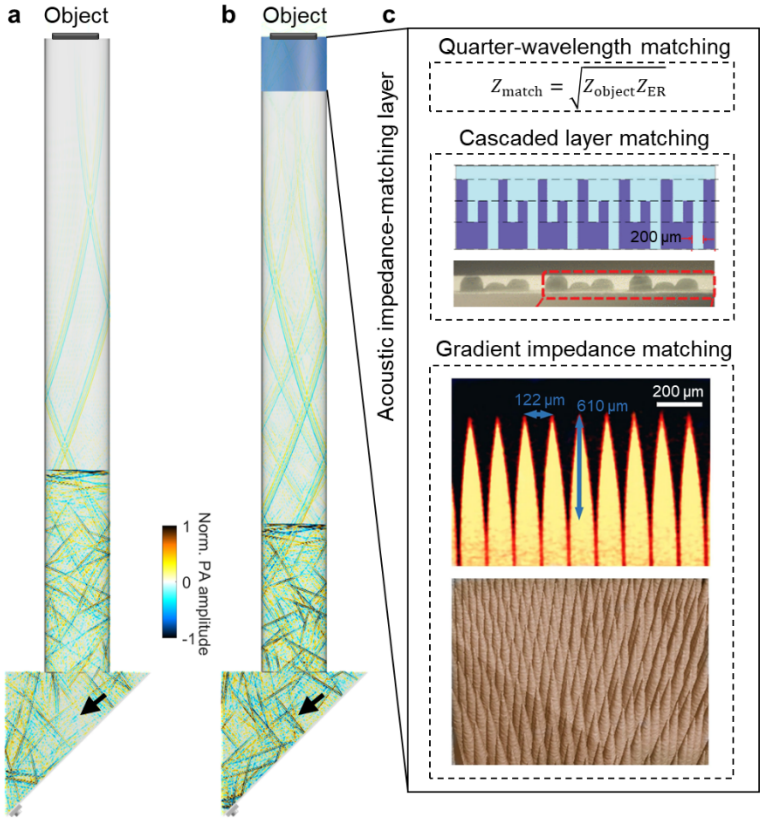

Supplementary Fig. 20 l Potential ways to improve the spatial resolution of PACTER.
a, Simulated PA signal propagating in the ER in PACTER. **b**, Simulated PA signal propagating in the ER with an acoustic impedance-matching layer between the object and the fused silica rod. A quarter-wavelength matching layer was used in the simulation. Black arrows in **a** and **b** show that the PA signal in **b** is stronger. **c**, Potential implementations of the acoustic impedance-matching layer in **b**. Top, acoustic impedance of the quarter-wavelength impedance-matching layer (Z_{match}), where Z_{object} and Z_{ER} are the acoustic impedances of the object and the ER, respectively. Middle, side view schematic and photograph of the cascaded impedance-matching layer[80]. Bottom, side view photography and 3D topography of the gradient impedance-matching layer[81].

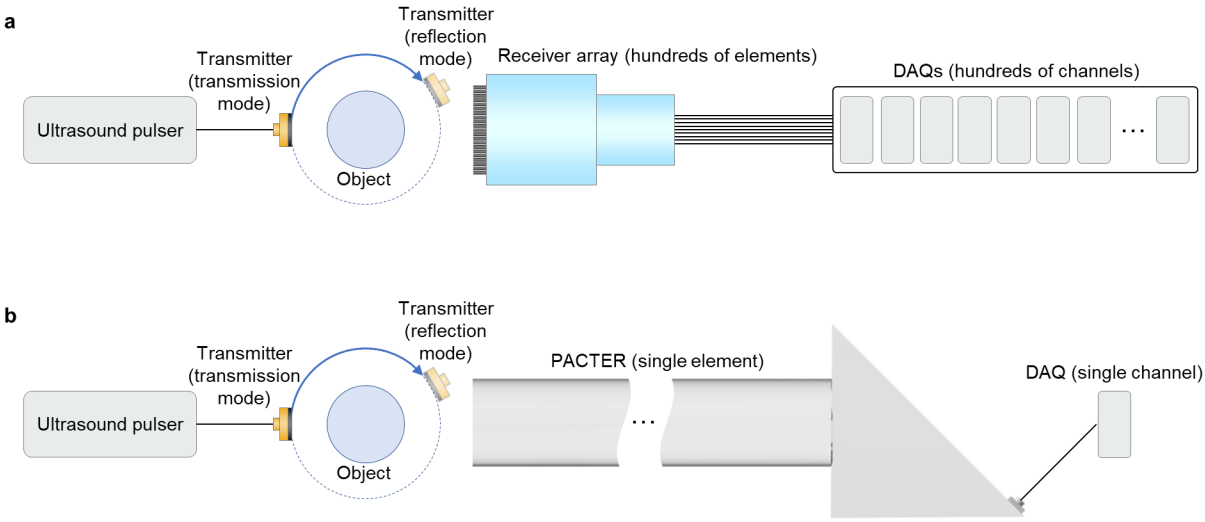

Supplementary Fig. 21 | Potential application of PACTER in ultrasonography.
a, Schematic of an ultrasonography system with a transmitter and a receiver array with hundreds of elements, which requires a DAQ device with hundreds of channels. The position of the transmitter can be adjusted to allow both transmission- and reflection-mode imaging[69]. **b**, Schematic of an ultrasonography system using PACTER. Compared with **a**, the receiver array is replaced by an ER with a single-element transducer, which requires a DAQ device with only a single channel.

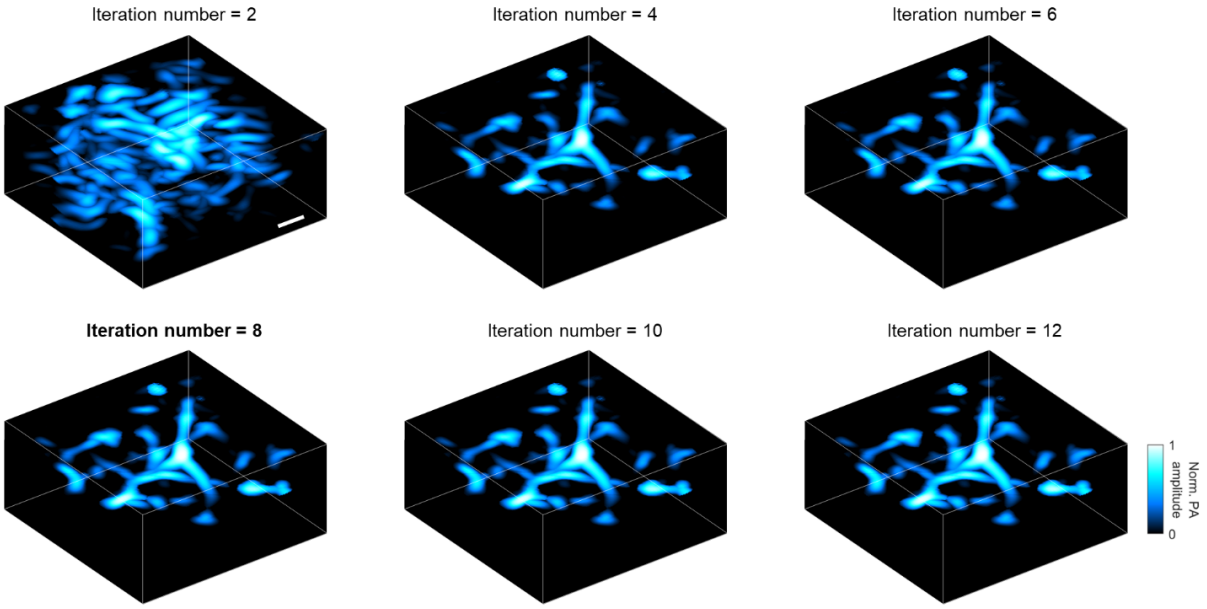

Supplementary Fig. 22 l Effect of the iteration number in the FISTA algorithm for PACTER reconstruction.
The imaging data were acquired form the thenar vasculature of participant 1. The image reconstruction times for iteration numbers 2, 4, 6, 8, 10, 12 were 167 s, 332 s, 494 s, 654 s, 819 s, 979 s, respectively. An iteration number of 8 (bolded fonts) was used in all PACTER reconstruction in this study. Norm., normalized. Scale bar, 1 mm.

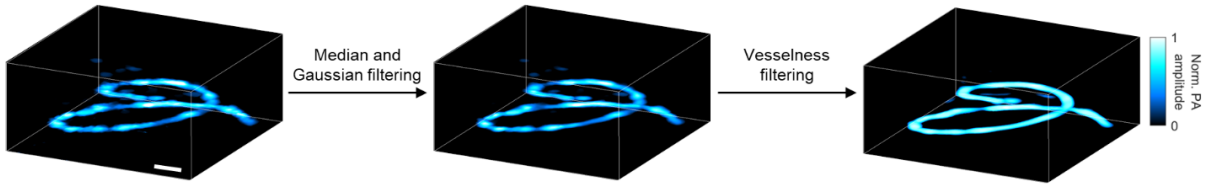

Supplementary Fig. 23 l Effect of the image processing filters on PACTER images.
The imaging data were acquired form a curved black wire. The raw reconstructed image (left) was first processed by 3D median and Gaussian filters (middle) and then applied with a Hessian-matrix-based vesselness filter (right). Norm., normalized. Scale bar, 1 mm.

Supplementary Table 1 | Comparison of PACTER and previous techniques using ERs.

	PATER[38]	PAMER[39]	PAISE[41]	PACTER
Universal calibration	No	No	Yes	**Yes**
Long-term stability	No	No	No	**Yes**
Single-shot 2D imaging	Yes	No	Yes	**Yes**
Single-shot 3D imaging	No	No	No	**Yes**
4D imaging	No	No	No	**Yes**
Thin object requirement	No	No	Yes	**No**
Transducer coupling	Post-fabrication (resin)	Post-fabrication (resin)	Post-fabrication (resin)	**Integrated (metallic)**
Transducer sensitivity	Low	Low	Low	**High**
Reconstruction algorithm	TwIST	TwIST	TwIST	**FISTA & FFT**
Animal imaging	Yes	Yes	No	**Yes**
Human imaging	No	No	No	**Yes**
Clinical applicability	No	No	No	**Yes**

Supplementary Video 1 | Principle and implementation of PACTER (with narration).

Supplementary Video 2 | Simulation of PATER and PACTER signals.
Simulation of PA wave propagation in the ERs in PATER (left) and PACTER (right) and the PA signals detected by the ultrasonic transducers attached to or fabricated on the cavities. The object-independent signal over a sufficient duration in PACTER enables object-independent universal calibration. Norm., normalized.

Supplementary Video 3 | 4D PACTER image and its maximum amplitude projection of bovine blood flushing through an S-shaped tube.
Norm., normalized.

Supplementary Video 4 | 4D PACTER images of bovine blood flowing through a tube at different speeds.
Norm., normalized.

Supplementary Video 5 | 4D PACTER image and its maximum amplitude projection of bovine blood flowing through a tube with a speed of 272.5 mm/s, captured at 1,000 volumes per second.
Norm., normalized.

Supplementary Video 6 | 4D *in vivo* PACTER image of the abdominal vasculature of mouse 1.
Top-left, 4D *in vivo* PACTER image. Norm., normalized. Top-right, 3D (2D in space and 1D in time) cross-sectional image corresponding to the yellow rectangle. Middle, PA amplitudes along the yellow dashed line (1D image) versus time. Bottom, center positions (blue solid curve) and widths (orange dash-dotted curve) of the vessel profiled by the yellow dashed line versus time. The shaded areas denote the standard deviations (n = 5).

Supplementary Video 7 | 4D *in vivo* PACTER image of the abdominal vasculature of mouse 2.
Top-left, 4D *in vivo* PACTER image. Norm., normalized. Top-right, 3D (2D in space and 1D in time) cross-sectional image corresponding to the magenta rectangle. Middle, PA amplitudes along the magenta dashed line (1D image) versus time. Bottom, center positions (blue solid curve) and widths (orange dash-dotted curve) of the vessel profiled by the magenta dashed line versus time. The shaded areas denote the standard deviations (n = 5).

Supplementary Video 8 | 4D *in vivo* PACTER image of the abdominal vasculature of mouse 3.
Top-left, 4D *in vivo* PACTER image. Norm., normalized. Top-right, 3D (2D in space and 1D in time) cross-sectional image corresponding to the yellow rectangle. Middle, PA amplitudes along the yellow dashed line (1D image) versus time. Bottom, center positions (blue solid curve) and widths (orange dash-dotted curve) of the vessel profiled by the yellow dashed line versus time. The shaded areas denote the standard deviations (n = 5).

Supplementary Video 9 | 4D *in vivo* PACTER image of the thenar vasculature of participant 1.
Top-left, 4D *in vivo* PACTER image. Norm., normalized. Top-right, maximum amplitude projection of the 3D volume. Middle, PA amplitudes along the yellow dashed line (1D image) versus time. Bottom, total PA amplitude (sum of all voxel values along the dashed line) versus time. The shaded areas denote the standard deviations (n = 5). The orange and cyan dashed vertical lines indicate the start times of occlusion and recovery, respectively.

Supplementary Video 10 | 4D *in vivo* PACTER image of the thenar vasculature of participant 2.
Top-left, 4D *in vivo* PACTER image. Norm., normalized. Top-right, maximum amplitude projection of the 3D volume. Middle, PA amplitudes along the magenta dashed line (1D image) versus time. Bottom, total PA amplitude (sum of all voxel values along the dashed line) versus time. The shaded areas denote the standard deviations (n = 5). The orange and cyan dashed vertical lines indicate the start times of occlusion and recovery, respectively.

Supplementary Video 11 | 4D *in vivo* PACTER image of the thenar vasculature of participant 1 in a different region.
Top-left, 4D *in vivo* PACTER image. Norm., normalized. Top-right, maximum amplitude projection of the 3D volume. Middle, PA amplitudes along the yellow dashed line (1D image) versus time. Bottom, total PA amplitude (sum of all voxel values along the dashed line) versus time. The shaded areas denote the

standard deviations (n = 5). The orange and cyan dashed vertical lines indicate the start times of occlusion and recovery, respectively.

Supplementary Video 12 | 4D *in vivo* PACTER image of the foot vessels of participant 3.
Top-left, 4D *in vivo* PACTER image. Norm., normalized. Top-right, difference between the maximum amplitude projections of the 3D volume and the first frame. The blue and orange circles indicate regions of a vein and an artery, respectively. Bottom, relative PA signals of the venous and arterial regions indicated by the blue and orange circles. The shaded areas denote the standard deviations (n = 5). The orange and cyan dashed vertical lines indicate the start times of occlusion and recovery, respectively.

Supplementary Video 13 | 4D *in vivo* PACTER image of the foot vessels of participant 3 in a different region.
Top-left, 4D *in vivo* PACTER image. Norm., normalized. Top-right, difference between the maximum amplitude projections of the 3D volume and the first frame. The blue and orange circles indicate regions of a vein and an artery, respectively. Bottom, relative PA signals of the venous and arterial regions indicated by the blue and orange circles. The shaded areas denote the standard deviations (n = 5). The orange and cyan dashed vertical lines indicate the start times of occlusion and recovery, respectively.

Supplementary Video 14 | PACTER signals affected by temperature fluctuations.
Top, PACTER signals acquired using bovine blood while the ER was periodically heated by a hot air gun. Middle, zoomed-in view of the signals in the black box in relation to the initial signal acquired at 0 s shown as purple dotted line. Bottom, correlatisson coefficient between the PACTER signal and the initial signal versus time. The orange dashed curve denotes the ON and OFF status of the hot air gun.

Supplementary references

74. Zimmermann, M., Lindlein, N., Voelkel, R. & Weible, K. J. Microlens laser beam homogenizer: from theory to application. *Laser Beam Shap. VIII* **6663**, 666302 (2007).
75. Treeby, B. E. & Cox, B. T. k-Wave: MATLAB toolbox for the simulation and reconstruction of photoacoustic wave fields. *J. Biomed. Opt.* **15**, 021314 (2010).
76. Saleh, B. E. A. & Teich, M. C. *Fundamentals of Photonics*. (Wiley-Interscience, 2007).
77. Abou-Sayed, A. S. & Clifton, R. J. Pressure shear waves in fused silica. *J. Appl. Phys.* **47**, 1762–1770 (1976).
78. Szabo, T. L. *Diagnostic Ultrasound Imaging: Inside Out*. (Elsevier, 2014).
79. Kino, G. S. *Acoustic Waves: Devices, Imaging, and Analog Signal Processing*. (Prentice-Hall, 1987).
80. Zhao, J. *et al.* Ultrawide Bandwidth High-Frequency Ultrasonic Transducers With Gradient Acoustic Impedance Matching Layer for Biomedical Imaging. *IEEE Trans. Ultrason. Ferroelectr. Freq. Control* **69**, 1952–1959 (2022).
81. Li, Z. *et al.* Broadband gradient impedance matching using an acoustic metamaterial for ultrasonic transducers. *Sci. Rep.* **7**, 42863 (2017).